Intrusive and non-intrusive two-phase air-water measurements on stepped spillways

A physical study

Arosquipa Nina, Yvan; Shi, Rui; Wüthrich, Davide; Chanson, Hubert

Important note
To cite this publication, please use the final published version (if applicable).
Please check the document version above.

Intrusive and non-intrusive two-phase air-water measurements on stepped spillways: A physical study

Yvan Arosquipa Nina [a], Rui Shi [a], Davide Wüthrich [a,b], Hubert Chanson [a,*]

[a] *The University of Queensland, School of Civil Engineering, Brisbane, QLD 4072, Australia*
[b] *Presently: Delft University of Technology, Department of Hydraulic Engineering, 2600 Delft, the Netherlands*

ABSTRACT

Self-aerated free-surface flow studies have a more recent history compared to classical fluid dynamics. Traditional velocimetry techniques are adversely affected by the presence of gas–liquid interfaces. In the present study, detailed air-water flow measurements were performed in a highly turbulent free-surface flow, and three velocimetry approaches were applied: (a) centreline dual-tip phase-detection needle probe measurements at all step edges downstream of the inception location of free-surface aeration; (b) Optical Flow (OF) data based upon ultra-high-speed video movies through the left sidewall; and (c) Optical Flow (OF) data based upon ultra-high-speed video movies overlooking the self-aerated flow, in a direction normal to the pseudo-bottom formed by the staircase profile. The study was conducted in a steep channel and three stepped invert geometries were tested. The results highlighted both advantages and limitations of the three complementary metrologies in free-surface flows with strong turbulence. The dual-tip phase-detection probe delivered reliable interfacial velocity data, but in the form of point measurements. The sideview OF technique provided a great level of details of the cavity recirculation and shear zone between mainstream and cavity, but the data were unreliable for void fractions>0.30 and only limited to the sidewall region. The top view OF technique characterised the surface velocity field across the entire chute width, highlighting the occurrence of three-dimensional air-water surface patterns. One observed limitation of the OF was the requirements of a high frame rate (i.e. 10,000 fps or more) and high-quality light source. Overall, these measurement techniques provided complementary results for a better understanding of the physical behaviour of highly turbulent multiphase flows on stepped channels.

1. Introduction

Two-phase air-water free-surface flows have been studied relatively recently compared to classical fluid dynamics. Some early scholars, e.g. Leonardo Da Vinci, observed self-aeration in free-surface flows and discussed the effects, writing: "*Water which falls from a height into other water imprisons within itself a certain quantity of air*"; "*if (…) air is submerged with impetus it comes back out of the water*"; "*air can never of itself remain beneath the water but always wishes to be above*" [36]. Air entrainment in mountain rivers and rapids is commonly observed when the flow turbulence breaks the water surface, and air entrainment, spray, foam and complex air-water projections take place (Fig. 1). The first successful laboratory measurements were undertaken mid-20th century [25,43], and the classical prototype data set of Cain and Wood [10] and Cain and Wood [11] at the Aviemore dam spillway (New Zealand) is barely 40 years old. Historically, the air-water flow data

were collected with electrical probes and suction tubes [25,43]. The use of dual-tip phase-detection probes [10] enabled more reliable measurements, and has been most common in self-aerated flows [18]. Rao and Kobus [39], Falvey [26], Wood [45] and Chanson [16] provided some overview of the developments and applications.

In air-water flows, traditional velocimetry techniques, e.g. Prandtl-Pitot tube, particle image velocimetry (PIV), laser Doppler anemometry (LDA), are adversely affected by the presence of gas–liquid interfaces [33,24]. With void fractions and liquid fractions greater than about 1%-3%, the most reliable velocimetries are (a) volumetric techniques, e.g. Gamma ray, tomography, (b) phase-detection needle probes, and (c) properly-validated optical techniques [33,13,7]. Volumetric techniques are restricted to small size experiments and are not commonly used in hydraulic engineering. Phase-detection needle probes include the optical fibre probe and conductivity/resistivity probe [31,13,3,21]. The needle sensor size may typically be<0.1 mm in low

Fig. 1. Example of self-aerated flows: cascading self-aerated waters at Le Grand Remous, Gatineau River (Canada) looking downstream viewed from Le Pont Couvert Savoyard on 13 July 2002.

velocity flows, while high velocity flow measurements require sturdier probe sensors, with sizes typically between 0.1 and 1 mm [19]. New optical techniques allow qualitative observations, although quantitative data remain scarse because of limitations in the validation [40,5,35,6,48]. In highly aerated gas–liquid flows, one approach, i.e. the Optical Flow (OF), detects the changes in brightness due to reflectance difference associated with passages of air-water interfaces [7,53]. The OF technique has been recently applied to a range of air-water flows recorded through glass sidewalls, with experience demonstrating a number of challenging issues. Sidewall effects can induce a substantial reduction in void fraction, bubble count rate and interfacial velocity compared to centreline air-water flow data. Reductions of up to 20–30% were documented comprehensively using sidewall optical techniques [6,53]. The finding represents a major challenge for the applicability of any optical technique, e.g. OF, bubble image velocimetry (BIV), particle image velocimetry (PIV) and particle tracking velocimetry (PTV), based upon photographs and movies recorded through the sidewalls.

In the present study, detailed air-water flow measurements were undertaken in a highly turbulent free-surface flow, with three stepped inverts, and three velocimetry approaches were applied: (1) centreline dual-tip phase-detection needle probe measurements at all step edges downstream of the inception location of free-surface aeration; (2) Optical Flow (OF) data based upon ultra-high-speed video movies through the left sidewall; and (3) Optical Flow (OF) data based upon ultra-high-speed video movies overlooking the self-aerated flow, in a direction normal to the pseudo-bottom formed by the staircase profile. In absence of prototype data sets, a series of queries is: what is the most reliable velocimetry technique in self-aerated highly-turbulent free-surface flows? Are the top view OF data physically meaningful? To what elevation do the top view OF data correspond? The current work intends to provide answer to these issues, expanding and comparing earlier studies undertaken with one or two metrologies.

2. Physical facility, instrumentation and methodology

2.1. Presentation

Physical experiments were undertaken in a large-size steep spillway model with very calm inflow conditions, previously used by Zhang and Chanson [53]. The water was supplied by three pumps controlled by adjustable frequency AC motors. The steep section was controlled by an upstream broad crested weir, and the steep chute had twelve steps with a longitudinal slope $\theta = 45°$. The steep chute was 0.985 m wide, ending in a horizontal channel discharging into a sump. Three step cavity configurations were used corresponding to ratios of cavity length to depth $\lambda/k = 2.0$, 2.5 and 3.0, with λ and k defined in Fig. 2A. For all configurations, the vertical step height was h = 0.10 m (Fig. 2).

2.2. Instrumentation

A series of dual-tip phase-detection probes ($\emptyset = 0.25$ mm) were used for intrusive air-water flow measurements. The conductivity needle probes were manufactured at the University of Queensland and excited by an electronics with a response frequency >100 kHz. The probe signals were sampled at 20 kHz per sensor for 45 s. All phase-detection measurements were performed on the channel centreline and the translation of the probe in the direction normal to the flow direction was controlled by a fine adjustment traverse mechanism connected to a HAFCO™ digital scale unit.

Visual observations of cavity recirculation, mainstream flow and free-surface turbulence were conducted with a Phantom™ ultra-high-speed digital camera (v2011) equipped with a Carl Zeiss™ Planar T*85 mm f/1.4 lens or a Nikkor™ AF 50 mm f1.4. The camera is seen in Fig. 3A (Foreground). The lenses were selected because they produced images with negligible degree of barrel distortion, i.e. ~0.087% and ~1.3% respectively. The camera's recording frame rate was set at 20,000 fps in high definition (1280 × 800 pixels). For some experiments, the camera system was mounted beside the test section, perpendicular to the sidewall (Fig. 3A), recording the air-water flow properties next to the wall through the left sidewall. The camera was focused on the flow field about 3–4 mm from the sidewall, and the depth of field was approximately 15 mm for the selected lens aperture. The camera was rotated by 45° as shown in Fig. 3A. For other experiments, the camera was mounted above the flume, pointed perpendicular to the pseudo-bottom formed by the step edges (Fig. 3B). In all cases, the lighting was provided by an intensive light emitting diode (LED) array, model GS Vitec MultiLED (cold white 7700 lm), to maximise the light and illumination of the flow features. Past experiences at the University of Queensland showed that the optical flow data quality was very strongly correlated to the quality of the lighting, and that a lot of preliminary tests had to be carried away with the lighting, before high-quality experiments could be undertaken, even with powerful light emitting diode (LED) arrays [42,47].

2.3. Experimental conditions

The experiments were conducted for water discharges between 0.070 m³/s and 0.198 m³/s, corresponding to dimensionless discharges d_c/h between 0.8 and 1.6 and Reynolds numbers between 2.8×10^5 and 8.0×10^5, with d_c the critical flow depth: $d_c = (q^2/g)^{1/3}$, q the unit discharge and g the gravity acceleration. The air-water flow measurements focused on steady skimming flows, as illustrated in Fig. 2. For one flow condition, i.e. $d_c/h = 1.2$, the ultra-high-speed camera was used, recording either from the sideview through the left sidewall or from the top, i.e. in a direction normal to the pseudo-bottom formed by the step edges. For each step configuration, four movies were recorded for the sideviews and three movies for the top views.
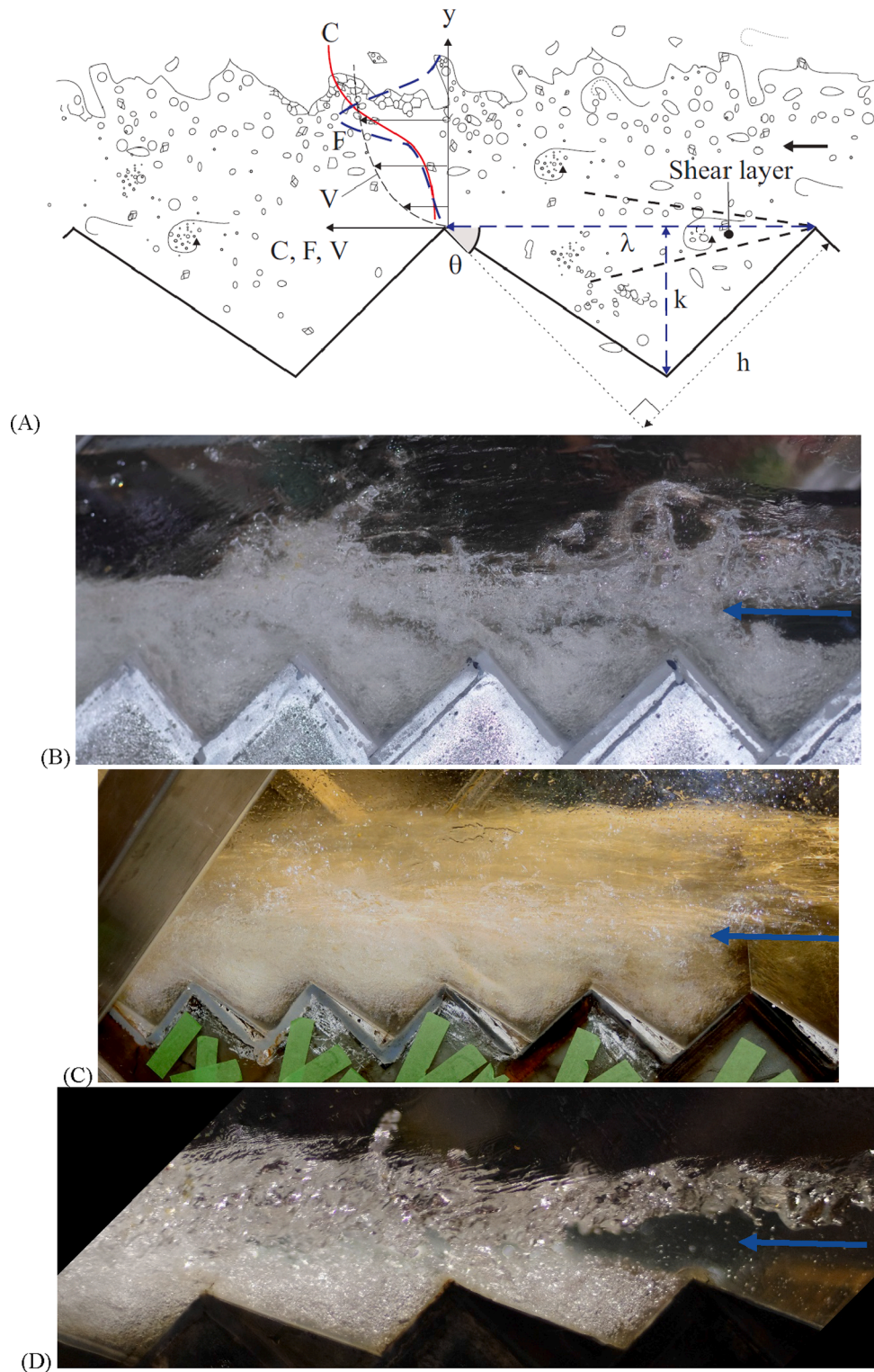
Fig. 2. Air-water flows above a 45° stepped chute with flow direction from right to left – (A) Definition sketch for $\lambda/k = 2.5$; (B-C-D) $d_c/h = 1.2$, Re $= 5.2 \times 10^5$, h $=$ 0.10 m, cavity aspect ratio: $\lambda/k = 2$ (B), 2.5 (C) and 3 (D).

3. Signal processing and analyses

3.1. Phase-detection probe signal analyses

The phase detection intrusive probe was manufactured with two identical tips based upon a needle tip design [38,18]. The recordings were performed at all step edges downstream of the air entrapment inception region using dual-tip conductivity probes which had a separation of probe tips $\Delta x_{tip} = 6.2$ mm in the longitudinal direction and $\Delta z_{tip} = 1.35$ mm in the transverse direction. The main parameters derived from the signal processing were the void fraction C, bubble frequency F, interfacial velocity V and turbulent intensity Tu [18].
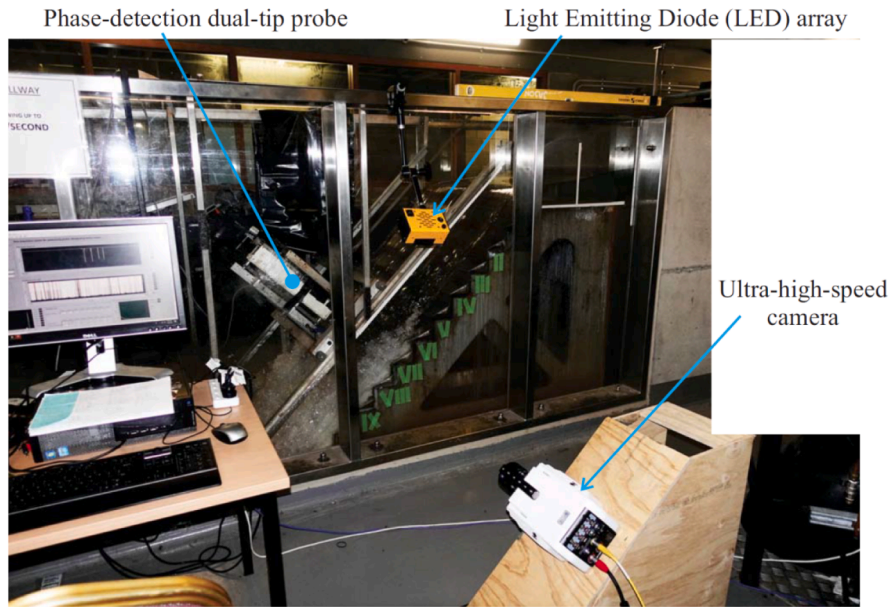
(A) Side view of the 45° stepped chute with the ultra-high-speed camera in the foreground and the phase-detection probe on the channel centreline - Flow conditions: $d_c/h = 1.2$, $Re = 5.2 \times 10^5$, $h = 0.10$ m, $\lambda/k = 2.5$
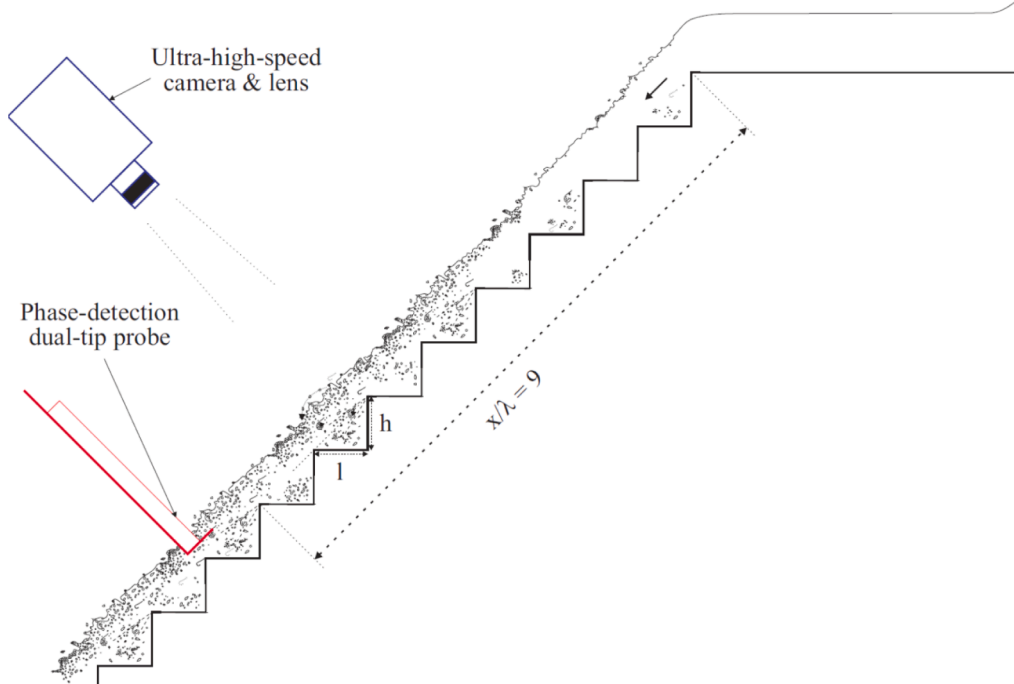
(B) Schematic of phase-detection probe and top-view ultra-high-speed video camera

Fig. 3. Air-water velocity measurements on the 45° stepped chute using intrusive and non-intrusive metrologies.

3.2. Optical flow (OF) technique

Major advances in image processing allow to compute air-water velocities in highly turbulent air-water flows based upon the optical flow techniques. The Optical Flow (OF) is a set of tools, detecting the flow motion between consecutive frames. Recently, the OF technique was applied to large-size free-surface flows, including self-aerated spillway flow [7,9,51,53]. Although different OF techniques were used among these studies, the governing equations were all based upon the assumption that the brightness constancy constraint [32]. Herein, the

OF technique proposed by Farneback [27] was used to compute the instantaneous velocity. The Farneback technique, also called Gunnar-Farneback technique, is a robust OF technique, in which the brightness data induced by the object motion from two consecutive frames followed quadratic polynomials. Full details on the implementation were reported in Arosquipa Nina et al. [2].

A sensitivity analysis of the processing parameters was performed on the OF longitudinal velocities, with a systematic comparison to the centreline dual-tip phase-detection probe (DTPDP) data. Several parameters affected the OF results, including the neighbourhood size,
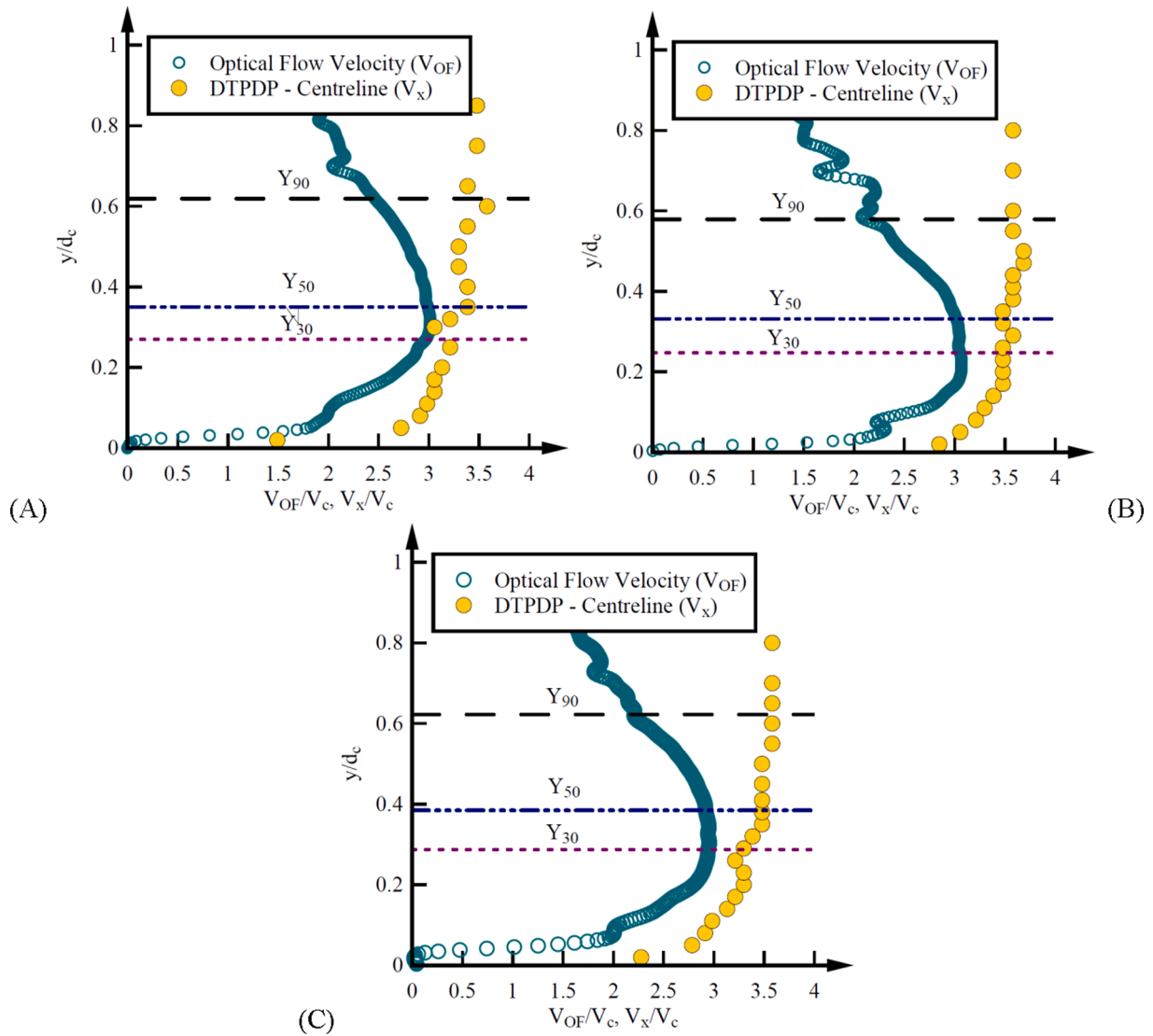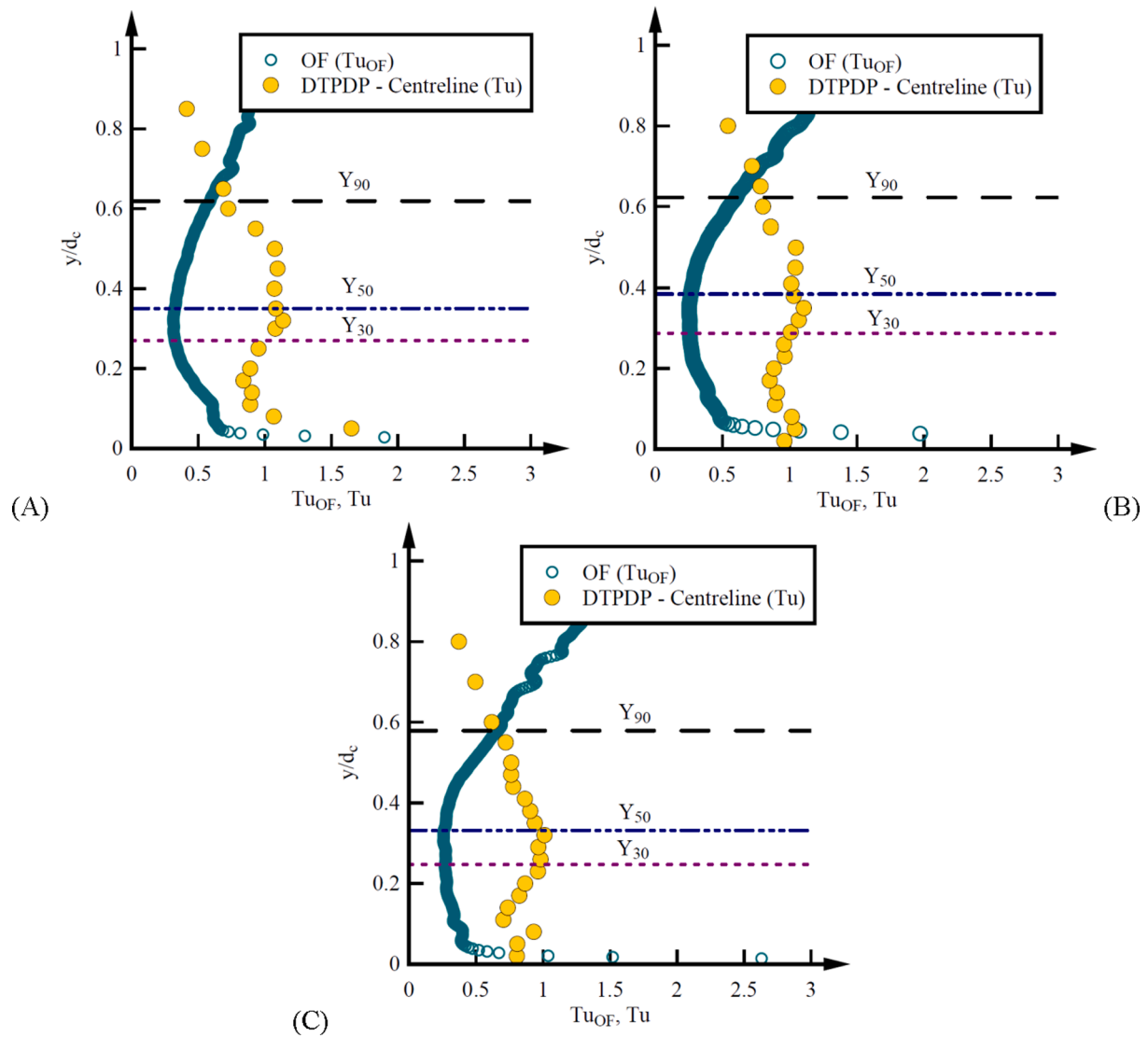
Fig. 4. Comparison between sideview optical flow (OF) and phase-detection probe velocity data – Symbols: V_{OF}: streamwise optical flow velocity, V_x: streamwise interfacial velocity, V_c: critical flow velocity – Flow conditions: $d_c/h = 1.2$, $x/\lambda = 8$ – (A) Horizontal steps ($\lambda/k = 2$); (B) 1 V:5H inclined steps ($\lambda/k = 2.5$); (C) 1 V:2.33H inclined ($\lambda/k = 3$); DTPDP: Dual-Tip Phase-Detection Probe, OF: Optical Flow.

filtering size and level of the image-pyramid. Note that the image pyramid is a subsampling technique to address large displacements in the OF technique [1]. Based upon the sensitivity analysis findings detailed by Arosquipa Nina et al. [2], the reference set of parameters included a neighbourhood-size of 5 pixels, an averaging filter-size of 15 pixels, an image pyramid with two levels and pyramid scale of 0.5. One-at-a-time method was applied, showing that a smaller neighbourhood-size led to a more accurate prediction of the velocity profiles and a greater filter-size resulted in a better prediction of the flow velocity profile when compared to the phase-detection probe data. Some sensitivity tests were also conducted in terms of the sampling rate, from 1000 Hz to 20,000 Hz. While Zhang and Chanson [53] recommended a minimum requirement of 5000 Hz, the current sensitivity test results showed that a minimum sampling rate of 10,000 Hz was required for a reasonable agreement with the dual-tip phase-detection probe data.

The same OF parameters were applied to both sideview and top view data sets. In addition, the OF data were averaged over four movies for the sideviews and three movies for the top views, each movie corresponding to a duration of 2.498 s.

3.3. Comparison between OF and phase-detection probe interfacial velocity data

The sideview optical flow velocity data (V_{OF}) were extracted at the locations (x,y) of the leading tip of the phase-detection probe, with x the longitudinal co-ordinate and y the distance normal to the pseudo-bottom formed by the stepped edges. Typical OF results are compared to the dual-tip phase-detection probe (DTPDP) interfacial velocity data (V_x) recorded on the channel centreline in Fig. 4. For completeness, the characteristic elevations Y_{30}, Y_{50} and Y_{90} are shown in Fig. 4, with these elevations corresponding respectively to a void fraction C = 0.30, 0.50 and 0.90 recorded by the DTPDP. First, the OF data were typically 10% to 30% smaller than the phase-detection probe velocity data. The latter reference data were recorded on the channel centreline, and the lesser velocity next to the sidewall was likely caused by sidewall friction effects [5,6,53]. Second, the optical flow data only showed a good qualitative agreement with the phase-detection probe data for $y/Y_{30} < 1$ (i.e. C < 0.3), despite the OF velocities being smaller than the interfacial velocities. For $y/Y_{30} > 1$, some increasing discrepancy between OF and phase-detection probe velocity data were observed with increasing elevations and void fractions, because of optical artefacts and aberration linked to

Fig. 5. Comparison between sideview optical flow (OF) and phase-detection probe turbulence intensity data – Symbols: Tu_{OF}: streamwise optical flow turbulence intensity, Tu: streamwise interfacial turbulence intensity – Flow conditions: $d_c/h = 1.2$, $x/\lambda = 8$ – (A) Horizontal steps ($\lambda/k = 2$); (B) 1 V:5H inclined steps ($\lambda/k = 2.5$); (C) 1 V:2.33H inclined ($\lambda/k = 3$); DTPDP: Dual-Tip Phase-Detection Probe, OF: Optical Flow.

image noise, low intensity gradients and inclusion of non-interfacial information (e.g. liquid film on inner sidewall surface) [53,34]. For $y/Y_{50} > 1$ (i.e. $C > 0.50$), the sideview optical flow data were unreliable, as illustrated in Fig. 4. For completeness, some similar issue and discrepancy were reported with other sideview optical techniques [6,7].

Fig. 5 compares the (sideview) OF turbulence intensity (Tu_{OF}) to the interfacial turbulence intensity (Tu), the latter being recorded on the channel centreline. Again, the characteristic elevations Y_{30}, Y_{50} and Y_{90} are shown in Fig. 5 for completeness. The turbulence intensity data were not directly comparable, as the phase detection probe data Tu were typically larger than the OF turbulence intensities Tu_{OF}. Focusing on the air-water region $y/Y_{30} < 1$ (i.e. $C < 0.3$), the OF turbulent intensity distribution followed a general trend comparable to the phase-detection probe data. Namely, the turbulent fluctuations were the largest in the region of high vorticity next to the pseudo-bottom formed by the step edges (Fig. 5). For $y/Y_{50} > 1$ (i.e. $C > 0.50$), the OF data should be deemed un-reliable [8,53], because the OF turbulence intensity data were affected by optical artefacts and aberration.

The top view OF longitudinal velocity data were extracted at the location (x, z) of the leading tip of the phase-detection probe and compared to the characteristic air-water velocity V_{90} at that location (x,

z), with z the spanwise co-ordinate ($0 < z < 0.985$ m). Herein, V_{90} is the interfacial velocity at $y = Y_{90}$ where $C = 0.90$. Typical data are shown in Fig. 6, where the thick solid vertical (red) lines mark the position of the inception of free-surface aeration. Overall, the results (Fig. 6) showed some reasonable agreement downstream of the inception point of free-surface aeration, but a poor agreement in the non-aerated flow region (i.e. $x/\lambda < 5.5$–6). For completeness, the top view OF data were further compared to the ideal fluid flow velocity and the sideview OF velocity obtained at $y = Y_{90}$ (Fig. 6). The OF (top view) velocity data showed a qualitative agreement with the ideal fluid flow estimate, neglecting drag, while the side view OF velocity at $y = Y_{90}$ were drastically underestimated (see above). Further discussion on the differences between the top view and sideview OF data is developed below (Section 3.4).

3.4. Discussion on data quality, noise and errors: top view versus sideview OF data sets

While the same OF technique was used for both top view and sideview movies, the OF data quality was diversely affected. With sideview movies, the light reflection and refraction induced by the entrained air-
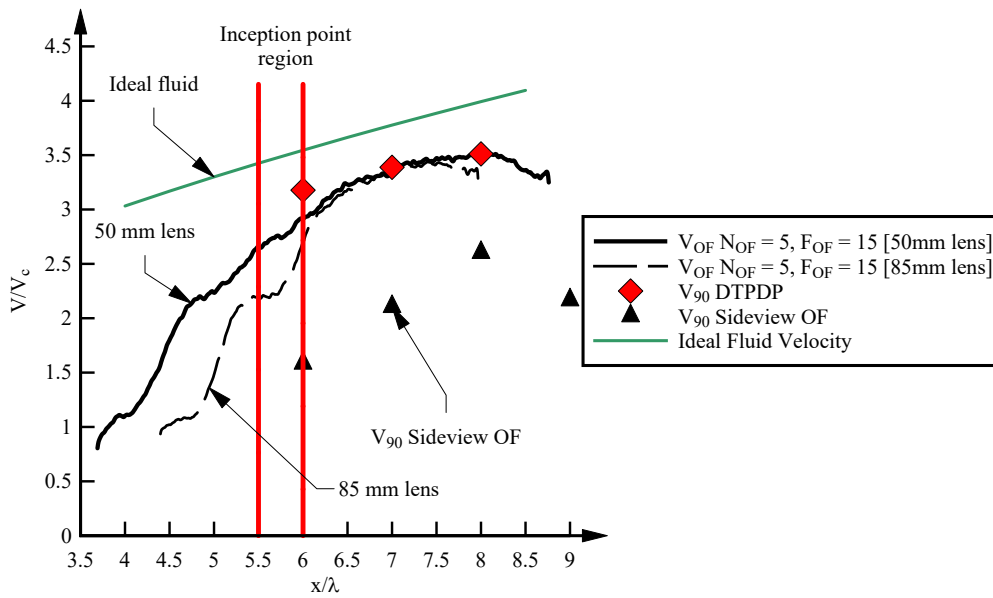
(A) Comparison between top view Optical Flow (OF), sideview OF and dual-tip phase-detection probe (DTPDP) velocity data - Symbols: V_{OF}: streamwise top view OF velocity, V_{90}: streamwise interfacial velocity at $y = Y_{90}$, V_c: critical flow velocity - Flow condition: $d_c/h = 1.2$, both 50 mm and 85 mm lens top view OF data are shown - Red vertical lines represent the inception region of free-surface aeration
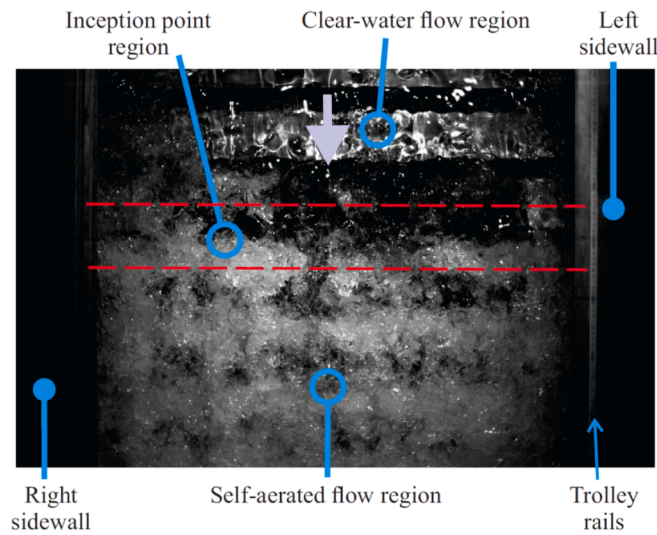
(B) Top view ultra-high-speed video image for $d_c/h = 1.2$, 1V:2.33V inclined steps, Nikkor™ AF 50mm f1.4 lens, with flow direction from top to bottom

Fig. 6. Comparison between top view OF and phase-detection probe characteristic velocity.

water features next to the free-surface caused optical artefacts, leading to some violation of the brightness constancy assumption. Further, some flow patterns and optical features appeared intermittently in the upper region. Simply, the OF sideview data were unreliable for C > 0.50, and they showed biased departures from the dual-tip phase-detection probe (DTPDP) data for C > 0.30 (Fig. 4), in line with previous OF results in stepped spillways [51,53].

For the top view movies, the images included the upstream non-aerated free-surface, the inception point region, and self-aerated free-surface downstream of the inception of free-surface aeration, as well as both sidewalls above the air-water free-surface (Fig. 6B). The optical artefacts were very different from the sideview movies. Optical reflections at the free-surface of the clear-water flow region, upstream of the inception region, led to meaningless outputs for x < L_I. The inception region was highly fluctuating, causing substantial noise. Further some edge effects were generated at the bottom end of the images and along both sidewalls. On another hand, the self-aerated flow region generated few artefacts in the top view movies, although the outputs lacked the
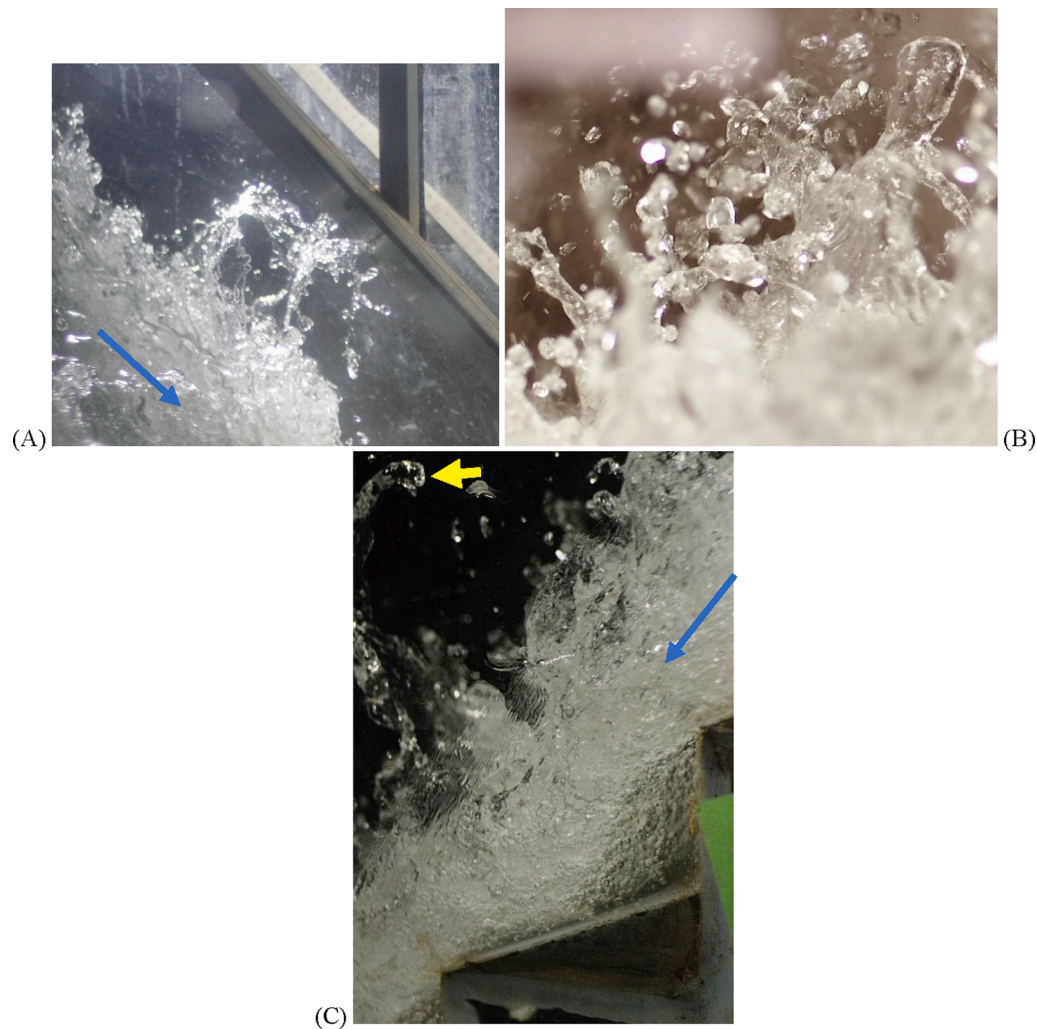
Fig. 7. Air-water entities projected in the upper free-surface on a 45° stepped chute – Light blue arrows show main flow direction. (For interpretation of the references to colour in this figure legend, the reader is referred to the web version of this article.)

third geometrical dimension (y). Namely, some un-answered questions are: at what elevation y was the OF data measured? and, how representative were the OF surface velocity data?

4. Basic air-water flow observations

4.1. Presentation

On the stepped chute, the upstream skimming flow was non-aerated and self-aeration was seen towards the downstream end the chute. The inception region was characterised by large free-surface fluctuations and a sudden free-surface aeration. Underneath the pseudo-bottom formed by the step edges, some strong cavity recirculation motion was maintained through some continuous transfer of momentum from the main stream to the cavity recirculation fluid, although the cavity ejection and replenishment process was irregularly observed. The movies M1, M2, and M3 (Digital Appendix I) present examples of cavity recirculation motion in stepped chutes with different cavity aspect ratios: $\lambda/k = 2.0$, 2.5 and 3.0 respectively. In the aerated flow region, some large amount of air-water entities were projected through the upper free-surface on the 45° stepped chute (Fig. 7 & Digital Appendix II). Some large quantities of fluid ejections were seen close to the inception point of free-surface aeration. Conversely, a complicated mix of fluid ejections and re-attachments were observed further downstream. Fig. 7 and Digital Appendix II present a number of high-speed photographs of air-water

features, photographically 'frozen' above the free-surface. Overall, the change in cavity shape impacted onto the cavity recirculation processes. The increased cavity aspect ratio λ/k induced some elongated asymmetrical cavity shape, with a less stable recirculation.

4.2. Void fraction and flow fragmentation

The upstream flow was non-aerated. When the turbulent fluctuations acting next to the free-surface were greater than the capillary resistance, the free-surface became rapidly aerated, as illustrated in Figs. 2, 3A and 6B. Downstream of the inception region, the local void fraction ranged from low values next to the bottom to 100% in the air above. At a given cross-section, the void fraction increased monotonically with increasing distance y from the invert. Typical data are presented in Fig. 8, where the measurements are shown in a self-similar fashion, with the void fraction C as a function of the dimensionless distance y/Y_{90} and Y_{90} the characteristic elevation where the void fraction was 0.9. For the lowest discharge ($d_c/h = 0.8$), the void fraction distributions exhibited relatively flat profiles (Fig. 8A & B). At large discharges ($d_c/h > 1.0$), the distributions of void fraction followed some S-shape, typically observed in smooth and stepped chutes [11,15,23]. In addition, the present data correlated well with some theoretical solutions [23], plotted in thick blue lines in Fig. 8.
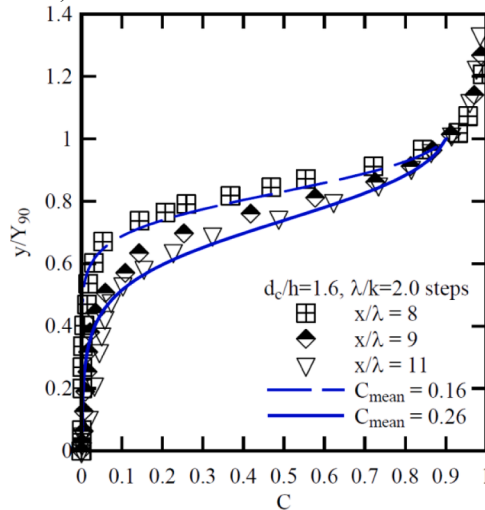
For a given void fraction, the bubble count rate is directly proportional to the fragmentation of the air-water flows. Typical distributions
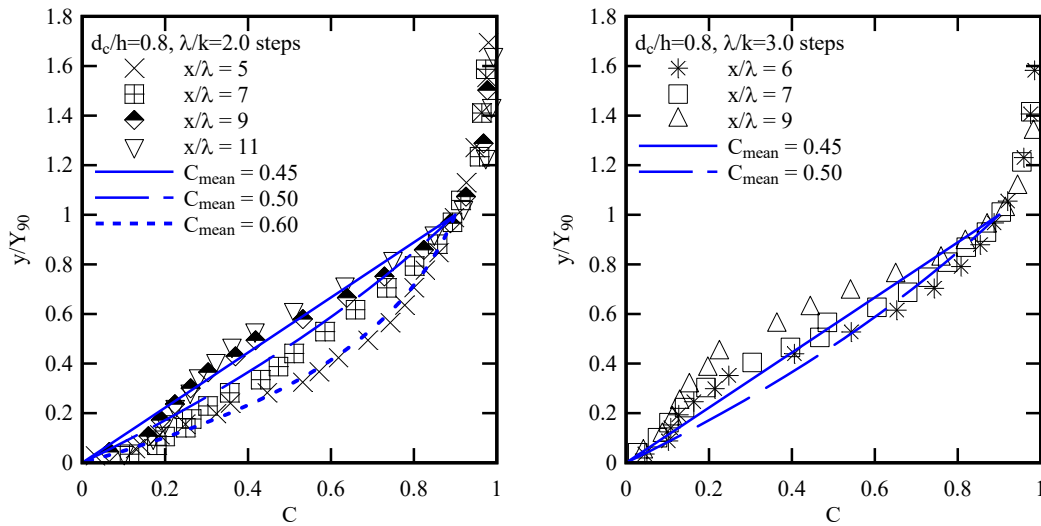
(A, Left) $d_c/h = 0/8$, $Re = 2.8 \times 10^5$, $\lambda/k = 2.0$

(B, Right) $d_c/h = 0/8$, $Re = 2.8 \times 10^5$, $\lambda/k = 3.0$

(C) $d_c/h = 1.6$, $Re = 8.0 \times 10^5$, $\lambda/k = 2.0$

Fig. 8. Dimensionless distributions of void fraction on a 45° stepped chute with flat horizontal and inclined steps – Legend provides detailed conditions.

are presented in Fig. 9. At a given location, the normal profiles showed a maximum value for a local void fraction between 0.3 and 0.5, and small bubble count rate next to both the invert and upper free-surface (Fig. 9A). Overall, the bubble count rates increased with increasing downstream distance from the inception of free-surface aeration, for a given flow condition. Since the inception region was shifting downstream with increasing discharge, the maximum bubble count rate at a given location x/λ decreased with increasing dimensionless discharge. Fig. 9B shows some typical longitudinal distributions of maximum bubble count rate. For all investigated flow conditions, the maximum bubble count rate data presented a marked monotonic increase, without an asymptotic value (Fig. 9B). Overall, the present findings in terms of bubble count rate were close to and similar to earlier investigations in air-water stepped chutes [23,30], Bung 2009, [4,44].

## 5. Two-phase air-water velocity measurements

5.1. Interfacial velocities (Phase-detection probe)

The interfacial velocity data were recorded based upon a cross-correlation analysis between the signals of the leading and trailing tips of the dual-tip phase-detection probe. All interfacial velocity data sets were measured at step edges on the channel centreline. Typical interfacial velocity profiles are shown in dimensionless form as V_x/V_{90} in Fig. 10, where V_{90} is the characteristic velocity at the elevation Y_{90}.
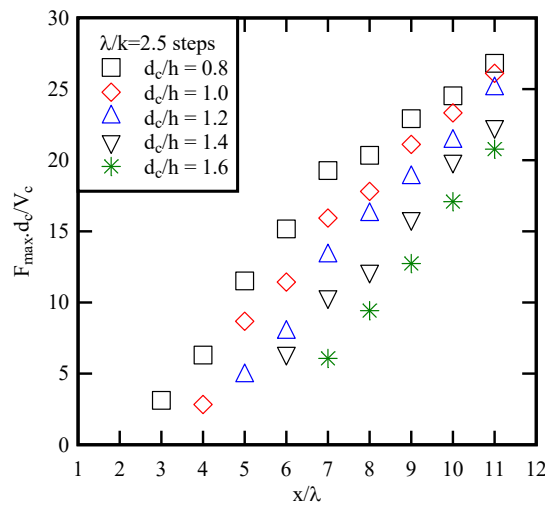
For all flow conditions, the interfacial velocity profiles showed some self-similarity, with a power law for $y < Y_{90}$ and a constant profile above:

$$\frac{V_x}{V_{90}} = \left(\frac{y}{Y_{90}}\right)^{\frac{1}{N}} \quad for \quad 0 \leqslant \frac{y}{Y_{90}} \leqslant 1 \tag{1A}$$

$$\frac{V_x}{V_{90}} = 1 \quad for \quad \frac{y}{Y_{90}} \geqslant 1 \tag{1B}$$
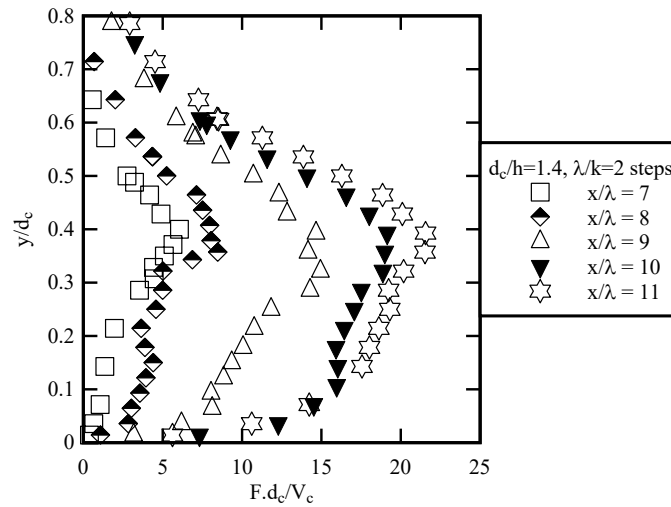
(A) Dimensionless distributions of bubble count rate $F \times d_c/V_c$ as function of y/d_c - $d_c/h = 1.4$, $Re = 6.5 \times 10^5$, $\lambda/k=2.0$

(B) Longitudinal distributions of maximum bubble count rate $F_{max} \times d_c/V_c$ - h = 0.10 , $\lambda/k=2.5$

Fig. 9. Dimensionless distributions of bubble count rate $F \times d_c/V_c$ on a 45° stepped chute – Legend provides detailed conditions.

The inverse N of velocity power law exponent varied between successive steps for all investigated conditions. Typical results are shown in Fig. 11, with N as a function of the dimensionless longitudinal distance x/λ. The see-saw fluctuation pattern was believed to be induced by the interferences between developing shear layers in the wake of each step edge and the cavity recirculation motion. Such a see-saw trend was previously reported in stepped chutes [12,29,28]. With the introduction of inclined steps, the change in cavity shape impacted onto the velocity magnitude, with larger depth-averaged velocities with larger cavity aspect ratio λ/k.

The turbulence intensity Tu gave some indication of the interfacial velocity fluctuations. Typical data are presented in Fig. 12 in skimming flows. For all stepped configurations, the vertical profiles presented a maximum about the location where the bubble count rate was maximum (Fig. 12A & B). At a given cross-section, the relationship between turbulence intensity and bubble count rate showed a monotonic trend, with increasing turbulence with increasing bubble count rate (Fig. 12C). In Fig. 12C, the experimental data are compared with trendlines (thick lines). The trend hinted a strong correlation between interfacial turbulence level and air-water flow fragmentation, hence air-water interfacial

area [23,28]. Some data scatter, together with some hysteresis, was observed in all stepped chute data.
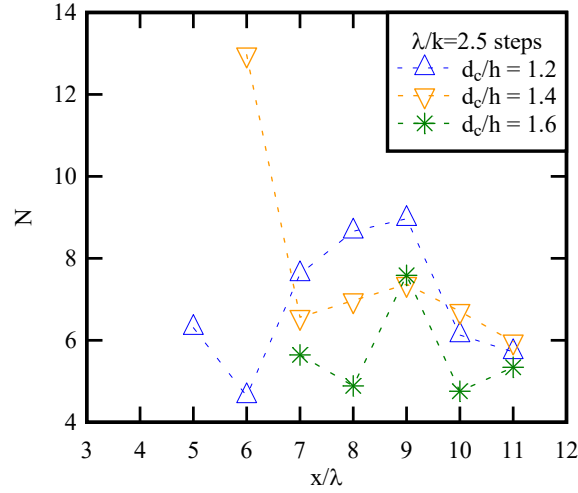
5.2. Optical flow (OF) data

The optical flow (OF) measurements were conducted with an ultra-high-speed digital camera, recording 20,000 fps in high definition (1280 × 800 pixels). For a series of experiments, the air-water flow properties were recorded next to the wall through the left sidewall (Section 5.2.1). For another series of experiments, the camera was mounted above the flume, pointed perpendicular to the pseudo-bottom formed by the step edges (Section 5.2.2). The data analyses were conducted for a dimensionless discharge $d_c/h = 1.2$, for which the inception of free-surface aeration was located at $x/\lambda \approx 5.5$–6. The whole OF data sets are reported in Arosquipa Nina et al. [2].

5.2.1. Sideview optical flow (OF) data

The sideview OF data focused on three step cavities, i.e. $6 < x/\lambda < 9$ for one flow rate: $d_c/h = 1.2$ and $Re = 5.2 \times 10^5$. Figs. 13 and 14 present the streamwise and normal optical flow velocities, i.e. V_x and V_y
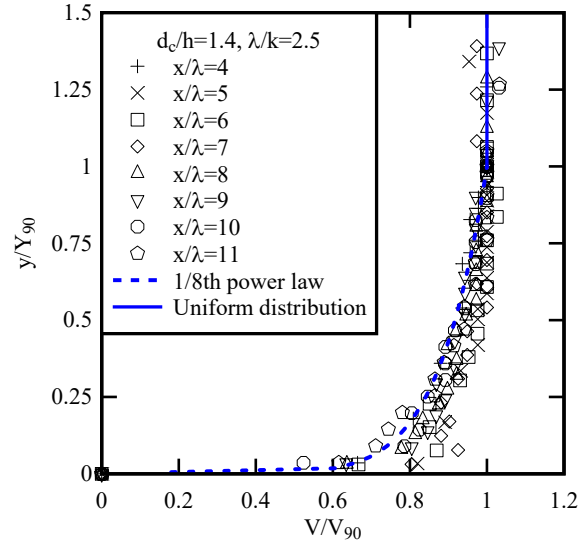
Fig. 10. Dimensionless distributions of interfacial velocities V/V_{90} on a 45° stepped chute (Centreline data at step edges) – $d_c/h = 1.2$, $Re = 5.2 \times 10^5$, h = 010 m, $\lambda/k = 2.5$ – Comparison with Eqs. (1A) and (1B).

Fig. 11. Longitudinal distributions of N in skimming flow on a 45° stepped chute ($\lambda/k = 2.5$) – Legend provides detailed conditions.

respectively, for all step configurations. The OF velocity data showed that the streamwise optical flow velocity V_x was small in the step cavities. In the main stream (i.e. $y > 0$), the streamwise velocity increased with increasing distance from the pseudo-bottom formed by the step edges (Fig. 13A, B & C). The trend was consistent with the phase-detection probe data, although the OF velocity data under-estimated the interfacial velocity for void fractions >0.30, as shown in Fig. 4. The normal optical flow velocity V_y data illustrated the recirculation in the step cavities and the flow interactions onto the treads of steps (Fig. 14A, B and C). For $\lambda/k = 2.0$, the normal OF velocity field showed a similar recirculation pattern within the two cavities located in $x/\lambda \approx 6.5$ and 8.5. In contrast, the middle cavity ($x/\lambda \approx 7.5$) presented a greater upward motion (Fig. 13A & A). The recirculation pattern was checked visually (and separately by several authors of this paper) in the video movies, replayed at several speeds. It was believed to be linked to the see-saw pattern in longitudinal distributions of characteristic air-water flow properties (e.g. V_{90}, F_{max}), observed in the present study and previously discussed by Yasuda and Chanson [49], Felder and Chanson [29], and Felder [28]. Fig. 14B shows an almost comparable normal fluid motion within all the cavities in the stepped chute with $\lambda/k = 2.5$. For $\lambda/k = 3.0$, the air-water mixture motion within the cavities differed

from the other stepped geometries (Fig. 14C). Altogether, the velocity data suggested that the momentum exchange between the mainstream and recirculation regions was affected by the cavity shape and aspect ratio, with a lesser recirculation volume, hence inertia, on the elongated step cavities. (For completeness, Figs. 13 and 14 include a few "spots" and "streaks" which were caused by the sidewall stains. These few spots were not noise from the OF technique.)

The streamwise and normal optical flow components provided further information on the visual deformation of the flow in different regions. The OF spanwise vorticity was calculated as

$$\omega_z = \frac{\partial V_y}{\partial x} - \frac{\partial V_x}{\partial y} \qquad (2)$$

where V_x and V_y are the streamwise and normal OF velocity components respectively, x is positive downstream and y is positive upwards, in the direction normal to the pseudo-bottom formed by the step edges. For all stepped configurations, the vorticity data presented little difference between the stepped geometries [2]. As a singularity, the step edges constituted the primary source of vorticity. Dimensionless vorticity $\omega_z \times d_c/V_c$ in excess of 5 were observed at the onset of the shear layer, in the
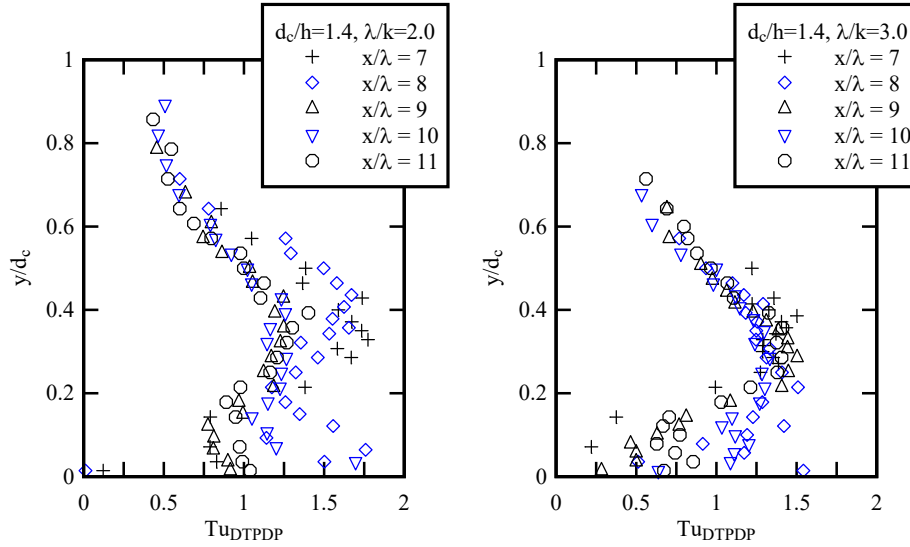
(A, Left) Dimensionless vertical profile for d_c/h = 1.4, Re = 6.5×10^5, and λ/k = 2.0

(B, Right) Dimensionless vertical profile for d_c/h = 1.4, Re = 6.5×10^5, and λ/k = 3.0
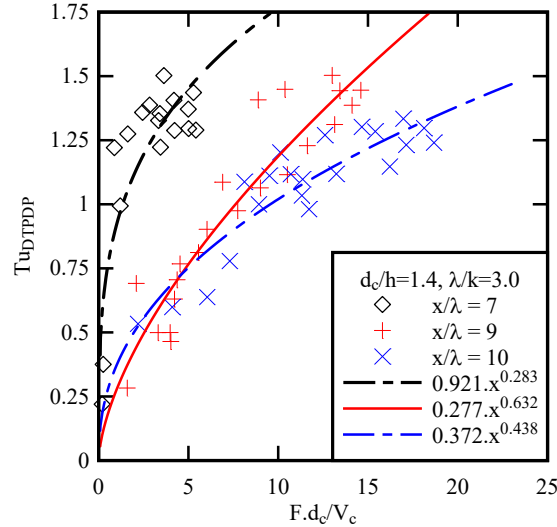
(C) Dimensionless relationship between interfacial turbulence intensity and bubble count rate for d_c/h = 1.4,

Re = 6.5×10^5, and λ/k = 3.0

Fig. 12. Dimensionless distributions of interfacial turbulence intensity Tu$_{DTPDP}$ in skimming flow on a 45° stepped chute – Legend provides detailed conditions.

near wake of each step edge. Further downstream, the vorticity diffused in the shear region up to the flow impingement on the next step edge. The present results were qualitatively and quantitatively similar to those of Zhang [50] with horizontal steps (λ/k = 2.0).

The Reynolds stresses provided informations on the velocity fluctuations in each direction. The OF Reynolds stress tensor components were calculated as:

$$\tau_{xx} = \rho \times v_x \times v_x \qquad (3)$$

$$\tau_{yy} = \rho \times v_y \times v_y \qquad (4)$$

$$\tau_{xy} = \rho \times v_x \times v_y \qquad (5)$$

where v_x and v_y are the streamwise and normal mean OF velocity fluctuations.

The Reynolds stress components presented some seminal features (Fig. 15). The higher magnitudes of dimensionless normal Reynolds stress τ_{xx} were found in the mainstream for the λ/k = 3.0 inclined step configuration, with comparatively higher fluctuation of velocity at the downstream end of the cavity (Fig. 15C). This might reflect upon a lesser momentum exchange between the elongated cavity recirculation and main flow. The Reynolds stress τ_{yy} data showed no significant difference between the three stepped configurations. The highest stresses were seen towards the downstream end of the step thread, where the developing shear layer interacted with the following step thread. The tangential Reynolds stress τ_{xy} components showed small differences between stepped configurations. The largest values were observed in the vicinity of the step edges.
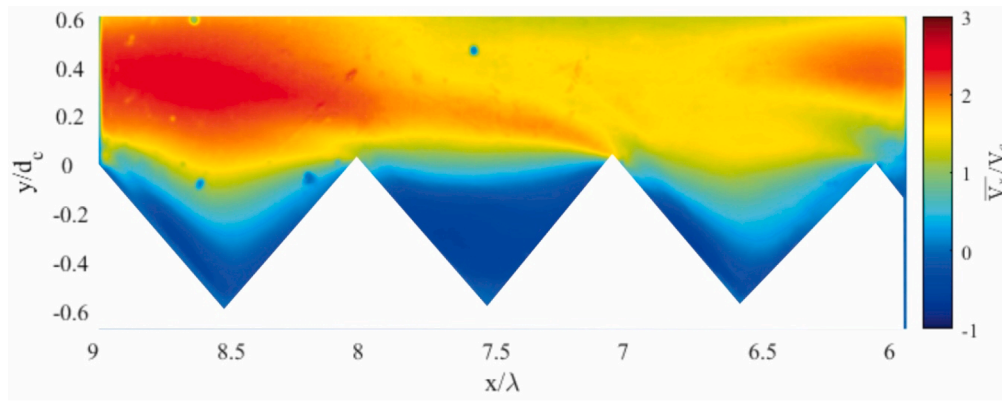
(A) Horizontal steps: λ/k =2.0
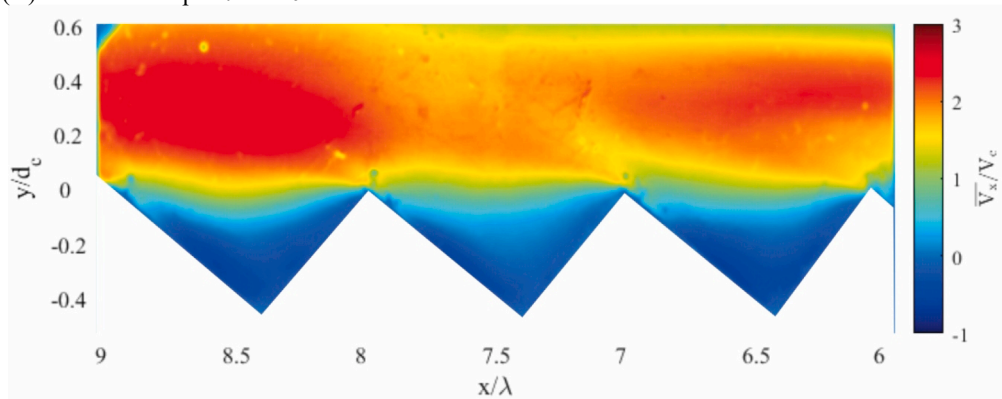
(B) Inclined steps: λ/k =2.5
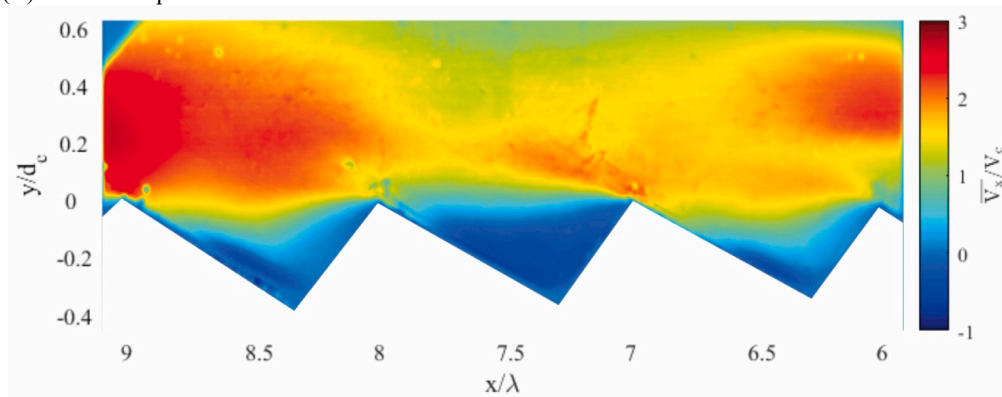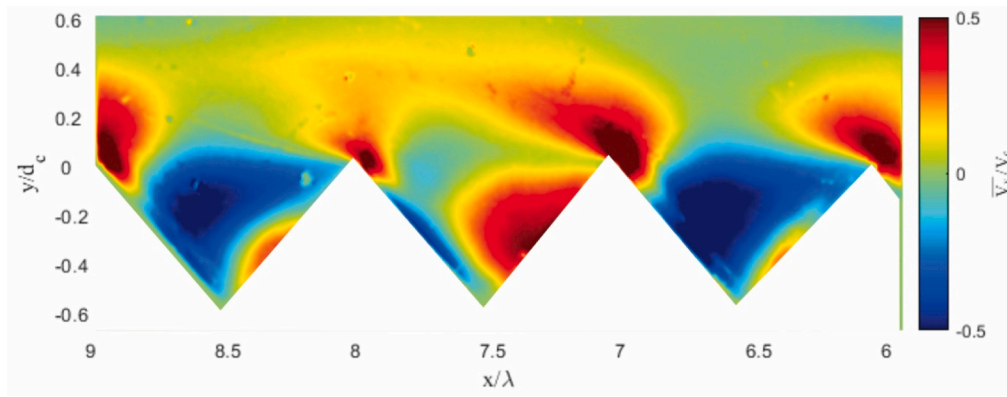

(C) Inclined steps: λ/k =3.0

Fig. 13. Dimensionless time-averaged streamwise optical flow velocity V_x/V_c for all stepped configurations – Positive results imply streamwise motion; negative values for motion against the flow direction – Main flow direction from right to left, camera focussed on step cavities 6–9, Pixel density: $\rho_{px}\,\rho_{px}$ = 29 px/cm, d_c/h = 1.2, Re = 5.2 × 10^5, θ = 45°, h = 0.10 m.

### 5.2.2. Top view optical flow (OF) data

First and foremost, the top view OF data characterised the longitudinal and spanwise motion of the upper surface of the self-aerated flow. While a similar approach was used in breaking bores [47], neither that study nor the present study could clearly ascertain the elevation of the OF data. The OF surface flow field provided some 'combined' description of the two-dimensional flow motion at different free-surface elevations, and "*did not represent a true continuous planar velocity field*". The current methodology delivered a qualitative and semi-quantitative

characterisation of the free-surface motion in a complicated highly-turbulent air-water flow. Further the results in the non-aerated flow are not reliable (Section 3.3).

Figs. 16 and 17 present the streamwise and transverse OF time-averaged velocities, i.e. V_x and V_z respectively, for all stepped configurations, where × is the streamwise direction positive downstream and z is the spanwise co-ordinate, with z = 0 at the right sidewall. (In the top view OF data, some horizontal lines appeared as velocity field discontinuity. These lines were the outer edges of the steps.) The location of the

(A) Horizontal steps: λ/k =2.0
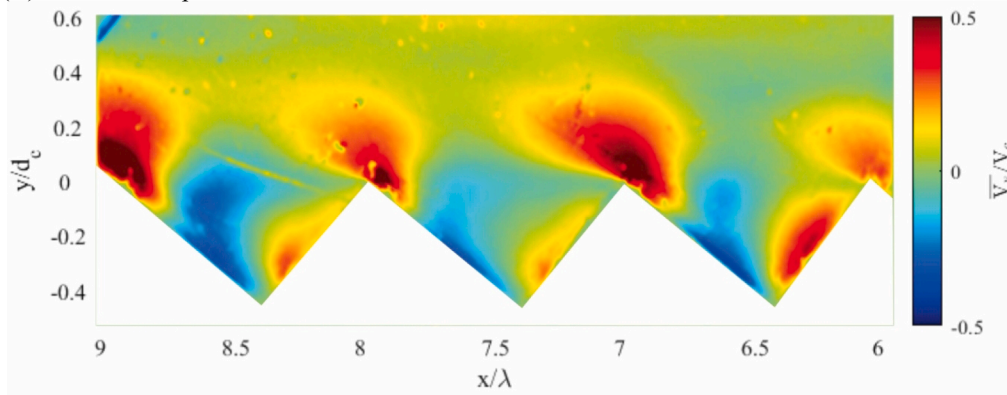
(B) Inclined steps: λ/k =2.5
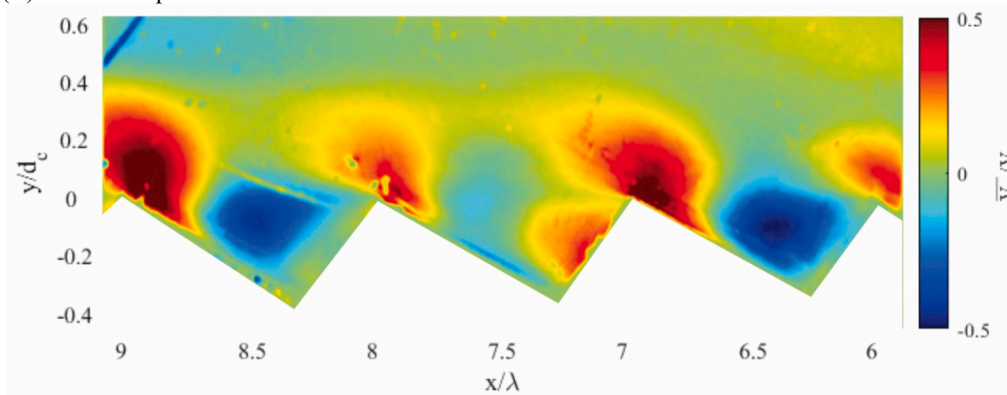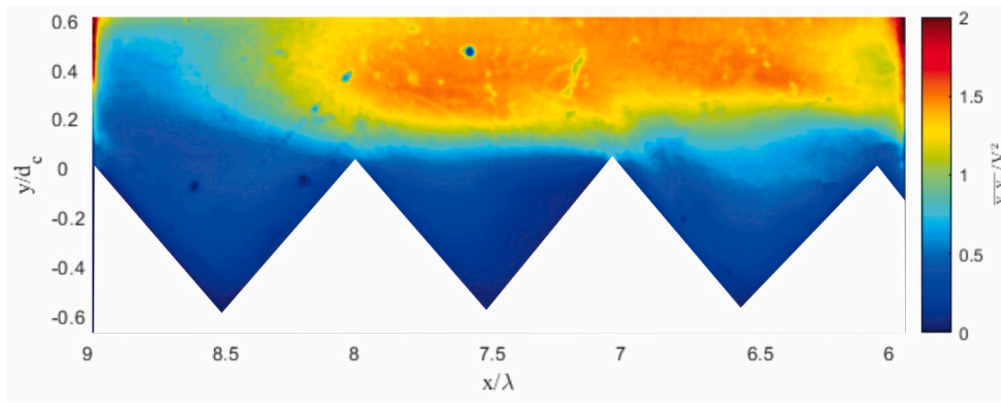

(C) Inclined steps: λ/k =3.0

Fig. 14. Dimensionless time-averaged normal optical flow velocity V_y/V_c for all stepped configurations – Positive results imply upward motion; negative values downward motion – Main flow direction from right to left, camera focused on step cavities 6–9, Pixel density: ρ_{px} ρ_{px} = 29 px/cm, d_c/h = 1.2, Re = 5.2 × 10^5, θ = 45°, h = 0.10 m.

inception point of entrainment was located at x/λ ≈ 5.5. to 6 for all configurations. Reflection effect (straight lines) could be seen at x/λ = 6, 7 and 8, corresponding to the outer edge of each step. Overall, the OF velocity data suggested that the streamwise optical flow velocity do not vary significantly between configurations (Fig. 16). The transverse OF velocity graphs illustrated no major difference between stepped geometries, with small transverse motion (Fig. 17). Larger values were observed in the vicinity of the sidewall, due to sidewall effect and no-

through flow boundary condition.

Both normal velocity data and tangential Reynolds stress τ_{xz} data showed some longitudinal structures downstream of the inception point, with 7 to 9 elongated structures across the entire chute width. These elongated air-water surface features were clearly seen visually, as illustrated in Fig. 18. Fig. 18 presents three high-shutter speed photographs, taken 120 ms apart. (For completeness, the photography did not show elongated air-water surface structures for shutter speed below 1/

(A) Horizontal steps: λ/k =2.0
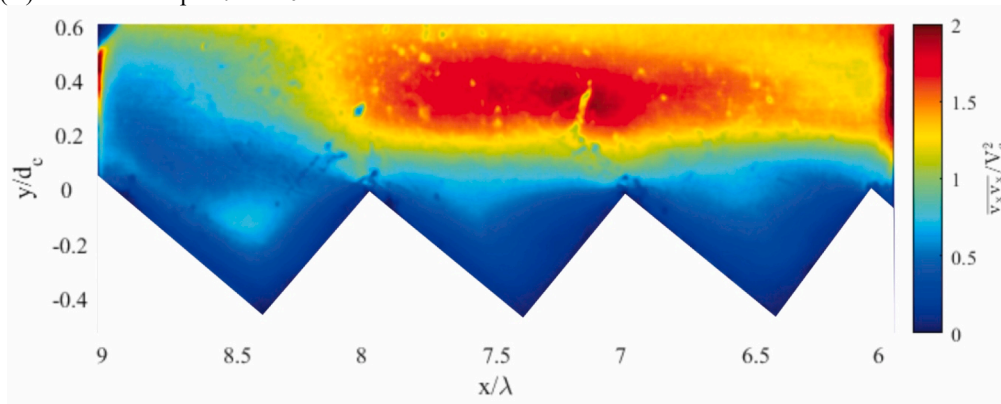
(B) Inclined steps: λ/k =2.5

(C) Inclined steps: λ/k =3.0

Fig. 15. Dimensionless optical flow normal Reynolds stress component in the flow direction $v_x \times v_x/V_c^2$ for all stepped configurations, with the camera focussed on step cavities 6–9 – Main flow direction from right to left, camera focussed on step cavities 6–9, Pixel density: $\rho_{px} = 29$ px/cm, $d_c/h = 1.2$, Re $= 5.2 \times 10^5$, $\theta = 45°$, h $= 0.10$ m.

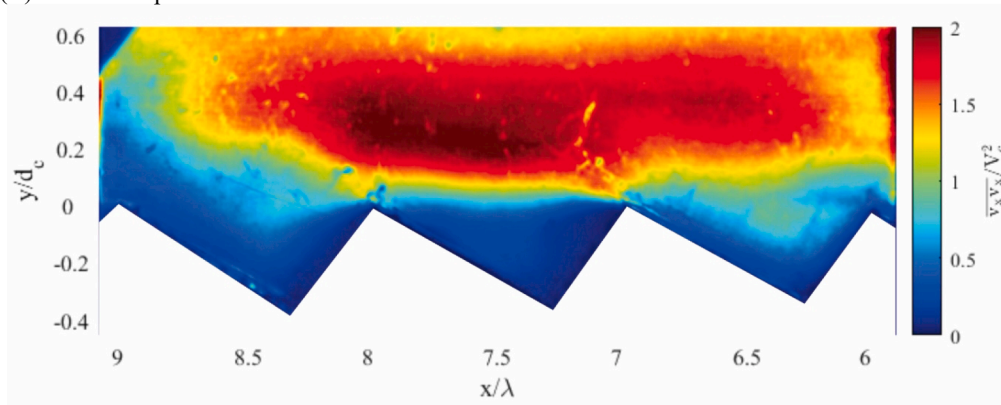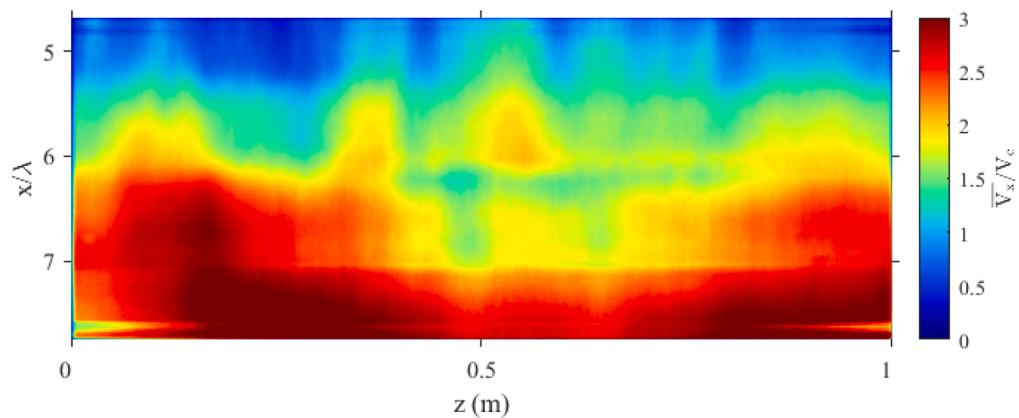1000 s, suggesting highly transient processes.) A total of 8 elongated white structures are visible in Fig. 18. Such air-water surface structures might be linked to the existence of three-dimensional recirculation cells in the step cavities next to and slightly downstream of the inception point of free-surface aeration, superbly evidenced by [37]. The transverse dimensions of the longitudinal structures were about $2 \times k$ to $2.3 \times k$. The present observations were close to surface scar sizes of about

$2.5 \times k$ to $2.8 \times k$ observed immediately upstream of the inception point at the Hinze dam spillway during a large overflow event [20]. These observations were conducted on 29 January 2013 for a discharge per unit width of $q \approx 14$ m^2/s ($d_c/h = 2.3$, Re $= 5.6 \times 10^7$). The surface scars were about 1.5–1. 7 m in size, immediately upstream of the inception point of free-surface aeration.

The OF spanwise vorticity ω_y data presented no significant difference

(A) Horizontal steps: λ/k =2.0 - ρ_{px} = 19 px/cm

(B) Inclined steps: λ/k =2.5 - ρ_{px} = 20 px/cm

(C) Inclined steps: λ/k =3.0 - ρ_{px} = 18 px/cm

Fig. 16. Dimensionless longitudinal optical flow surface velocity V_x/V_c for all stepped configurations – Positive results imply streamwise motion, whereas negative values for motion against the flow direction – Main flow direction from top to bottom, Pixel density as indicated in the sub-caption, d_c/h = 1.2, Re = 5.2 × 10^5, θ = 45°, h = 0.10 m.

(A) Horizontal steps: $\lambda/k = 2.0$ - $\rho_{px} = 19$ px/cm
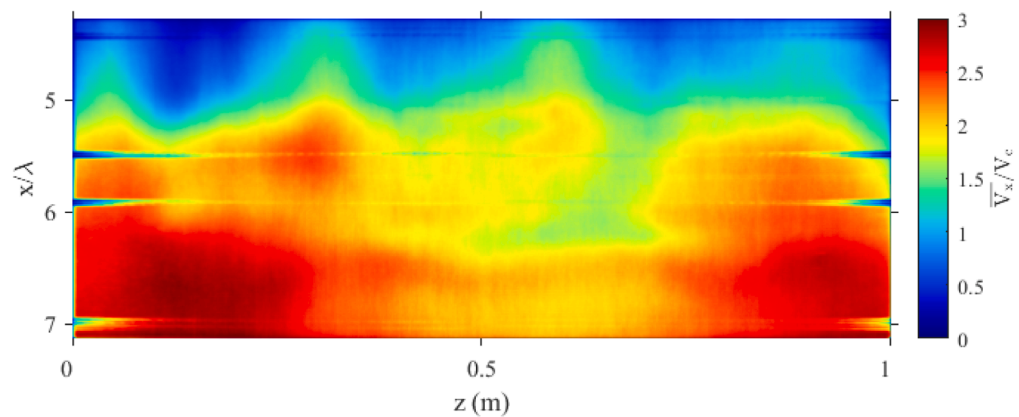
(B) Inclined steps: $\lambda/k = 2.5$ - $\rho_{px} = 20$ px/cm
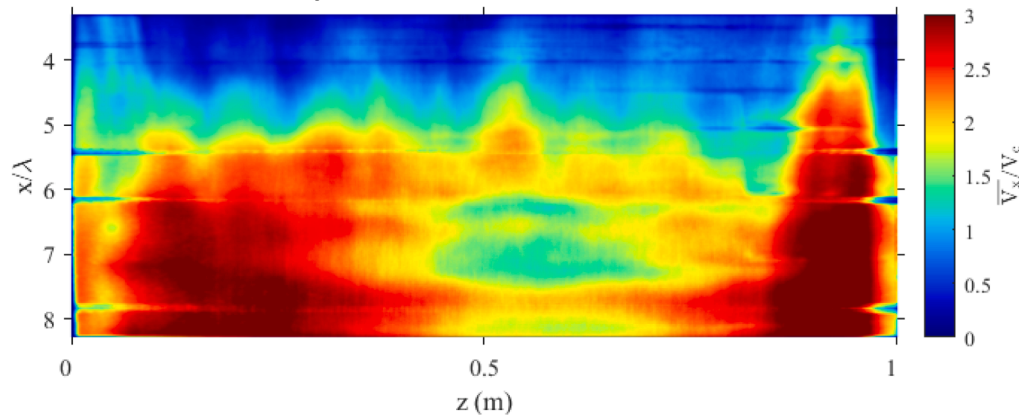
(C) Inclined steps: $\lambda/k = 3.0$ - $\rho_{px} = 18$ px/cm
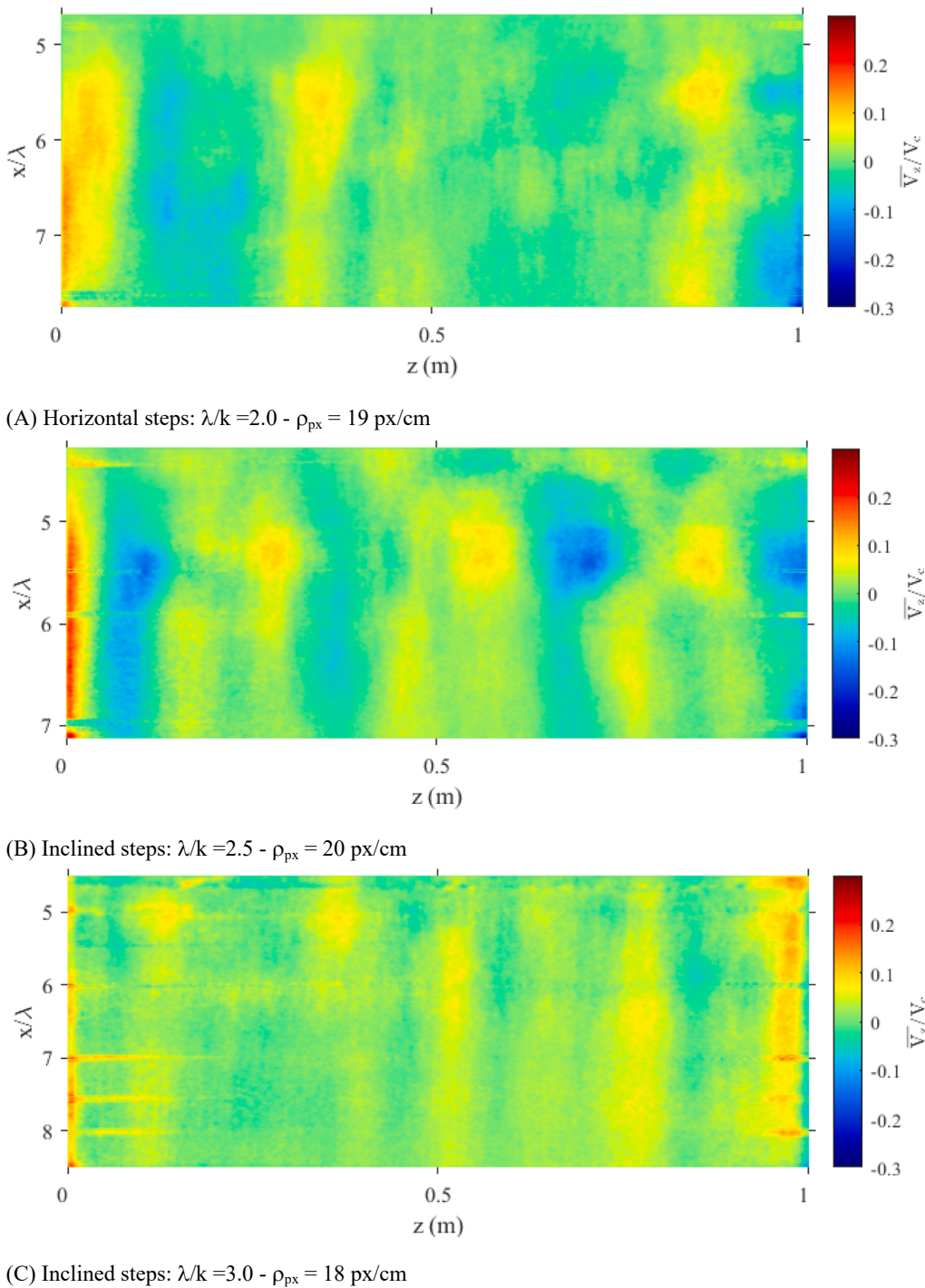
Fig. 17. Dimensionless spanwise (transverse) optical flow surface velocity V_z/V_c for all stepped configurations – Positive results imply motion towards the right sidewall, whereas negative values for motion the left sidewall – Main flow direction from top to bottom, Pixel density as indicated in the sub-caption, $d_c/h = 1.2$, Re $= 5.2 \times 10^5$, $\theta = 45°$, h = 0.10 m.

between configurations, although some reflection effect were observed on the outer edge of each step [2].

The Reynolds stress τ_{xx} data showed some similarity between the three stepped configurations (Fig. 19). The τ_{xx} data increased sharply at the inception region of free-surface aeration. Indeed, the inception point was a highly turbulent region, where the outer edge of the developing boundary layer interacted with the free-surface, and some flapping mechanism occurred [14,17]. Both present and past observations showed a violent aeration mechanism [20,52], conducive of large surface normal turbulent stresses. The present OF data suggested higher stress values in the inclined stepped chute data ($\lambda/k = 3.0$), in line with sideview OF results. The normal Reynolds stress τ_{zz} data showed no

Fig. 18. High-shutter speed top view photographs of skimming flow on the 45° stepped chute – Main flow direction from top to bottom, $d_c/h = 1.2$, Re $= 5.2 \times 10^5$, $\theta = 45°$, h = 0.10 m, $\lambda/k = 2.0$, 24 MPixels dSLR photographs, Shutter speed: 1/8000 s, with 120 ms between photographs (from left to right).

major difference between the three stepped geometries, although slightly higher values were found for the inclined stepped chute with $\lambda/k = 3.0$ next to the sidewalls (not presented here).

The dimensionless tangential Reynolds stress τ_{xz} data presented some surface stress maps that were symmetrical about the channel centreline, overall. The tangential Reynolds stress τ_{xz} data showed little difference between the stepped configurations (Fig. 20), although the data showed the existence of longitudinal air-water surface structures. These features were best seen in the top view OF data with the wider 50 mm lens ($\rho_{px} = 11$–12 px/cm). Note that slightly larger values of tangential stresses τ_{xz} were observed on the inclined stepped configuration with $\lambda/k = 3.0$.

5.3. Discussion on limitations and constraints of optical flow (OF)

The present experience showed a number of challenging issues with the application of OF to self-aerated chute flows, not always clearly documented in the literature:

(a) Sidewall effects were previously documented, with substantial reductions in void fraction, bubble count rate and interfacial velocity next to the sidewalls, compared to centreline data. Reductions in velocity of up to 20–30% were reported with phase-detection probes [51,53,46]. In turn, the optical flow velocity data based upon sideview recordings were not truly representative of the bulk flow velocity field.

(b) When the void fraction exceeded 30% to 50%, the (sideview) optical flow velocity data were not representative of the true interfacial velocities (Section 3.3). The sideview OF streamwise velocity data were much lower than phase-detection velocity probe data, with very large deficits for void fractions >50%. This issue was previously reported and discussed by others [7,53].

(c) The sidewalls acted as a boundary for the flow, not allowing any fluid motion to move through the wall, altering the air-water flow patterns in particular the recirculation motion in the step cavities, in the vicinity of the walls. More generally, any optical technique used for depth profiles, velocity data and air-water flow contain some intrinsic bias because of sidewall effects.

(d) It is unclear at what elevations the top view OF velocity field was recorded, with the top view movies. Wüthrich et al. [46] suggested that OF surface flow field provided a description of the

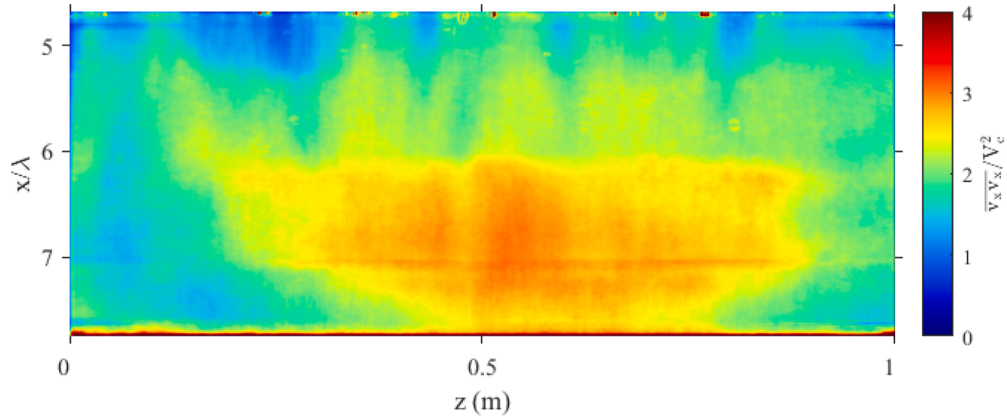two-dimensional free-surface flow motion across different free-surface elevations.

(e) The top view videos were adversely affected by light reflections from sidewalls and step edges. The optical spanwise vorticity results were a clear example of these effects. In turn, the physical significance of the top view velocity field remained difficult to fully comprehend.

(f) It is acknowledged that only one dimensionless discharge $d_c/h = 1.2$ was analysed for side and top view video movies.

(g) The video movies recorded with the 50 mm lens encompassed a wider domain, compared to the 85 mm lens, and the movie pictures were more impacted by step edge reflections.

(h) The duration of each video movie was about 2.5 s. The data were averaged over four movies for the sideviews and three movies for the top views, and all movies had similar means and standard deviations. Yet, the total recording time might not be long enough to document all air-water features and patterns, especially for the top view data. And the cumulative recording time was much shorter than the total sampling time of the dual-tip phase detection probe (45 s).

(i) The OF data quality was very strongly correlated to the quality of the lighting. A substantial amount of preliminary testing was required beforehand, to ensure high-quality data, even with the powerful light-emitting diode (LED).

Overall, the present observations and discussion on OF data added to an earlier pertinent discussion [22]. Despite a few challenges, the OF technique provided nicely some complementary data, in addition to dual-tip phase-detection probe measurements. The joint usage of both dual-tip phase-detection probe (DTPDP) and OF could be considered a natural metrology to document complicated self-aerated flows [53,41].

6. Conclusion

Detailed air-water velocity measurements were conducted in a steep stepped chute with three complementary approaches: (a) a dual-tip phase-detection probe sampling on the channel centreline at all step edges downstream of the inception point of free-surface aeration, (b) optical flow (OF) data obtained from sideview movies, between $6 < x/\lambda < 9$, and (c) top view OF data between $3.5 < x/\lambda < 9$.

The interfacial velocities V_{90} increased monotonically with increasing longitudinal distance for a given flow condition. For the same

(A) Horizontal steps: λ/k =2.0 - ρ_{px} = 19 px/cm

(B) Inclined steps: λ/k =2.5 - ρ_{px} = 20 px/cm
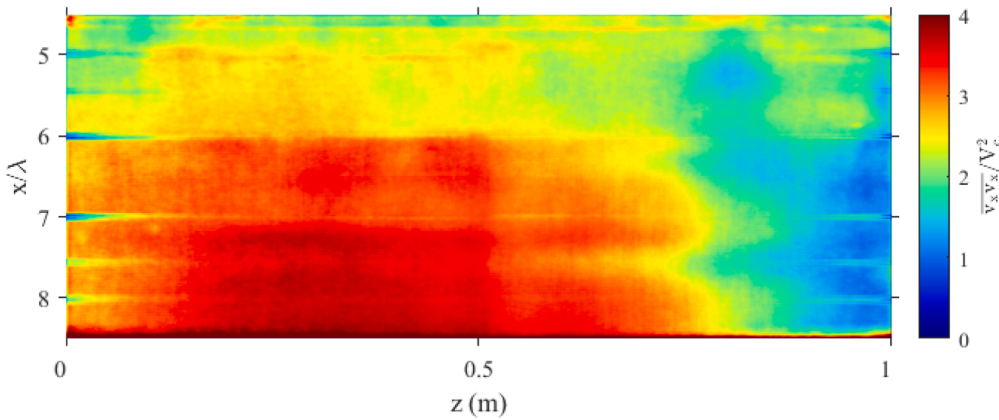
(C) Inclined steps: λ/k =3.0 - ρ_{px} = 18 px/cm

Fig. 19. Dimensionless optical flow Reynolds stress $v_x \times v_x/V_c^2$ for all stepped configurations – Main flow direction from top to bottom, Pixel density as indicated in the sub-caption, $d_c/h = 1.2$, Re = 5.2×10^5, θ = 45°, h = 0.10 m.

(A) Horizontal steps: λ/k =2.0 - ρ_px = 19 px/cm

(B) Inclined steps: λ/k =2.5 - ρ_px = 20 px/cm

(C) Inclined steps: λ/k =3.0 - ρ_px = 18 px/cm

Fig. 20. Dimensionless optical flow Reynolds stress $v_x \times v_z/V_c^2$ for all stepped configurations – Main flow direction from top to bottom, Pixel density as indicated in the sub-caption, $d_c/h = 1.2$, $Re = 5.2 \times 10^5$, $\theta = 45°$, $h = 0.10$ m.

discharge, the slowest velocities were observed on the horizontal stepped chute (λ/k = 2), with larger velocity with increased cavity aspect ratio λ/k. The interfacial turbulence intensity showed large t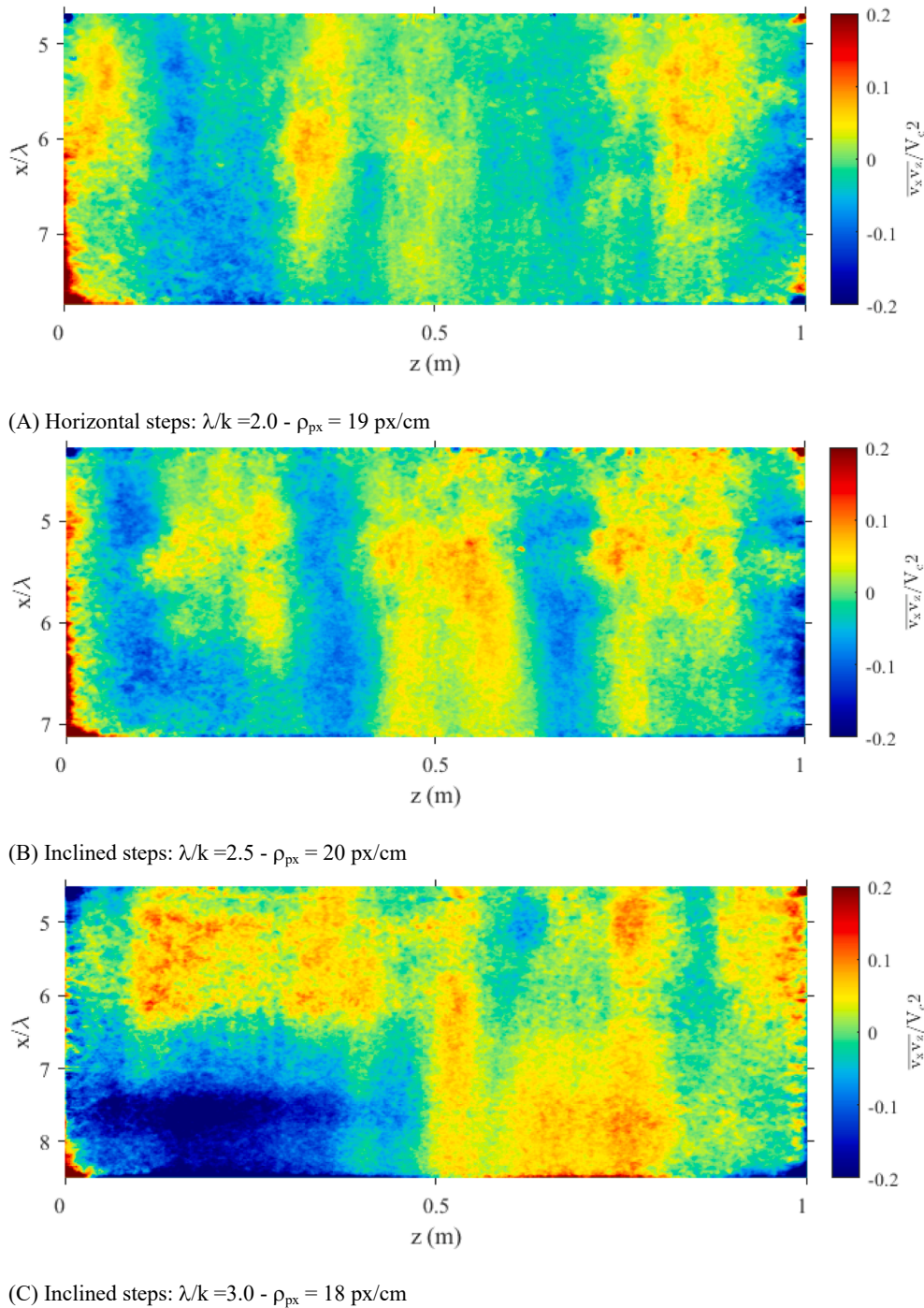urbulence levels, with a strong correlation between interfacial turbulence and bubble count rate, hence air-water flow fragmentation and air-water interfacial area.

The OF velocity results showed some difference in normal velocity field between three stepped configurations, suggesting that the momentum exchange between the mainstream and recirculation regions was affected by the cavity shape and aspect ratio, with a lesser recirculation volume on the inclined downward stepped chutes. The top view OF results highlighted the existence of longitudinal air-water structure downstream of the inception region, with 7 to 9 elongated structures across the entire chute width, their transverse dimensions being about 2 × k to 2.3 × k (i.e. 1.1 × h to 1.4 × h). These structures might be linked to three-dimensional recirculation cells in the step cavities next to and

slightly downstream of the inception of free-surface aeration.

Altogether, the study of highly-aerated turbulent free-surface flows showed both advantages and limitations of the three complementary metrologies. The dual-tip phase-detection probe (DTPDP) delivered reliable interfacial velocity data on the channel centreline, but in the form of point measurements with an intrusive approach. The sideview OF technique provided a great level of details of the cavity recirculation and shear zone between mainstream and cavity, but the data were unreliable for void fractions >0.3 and characterised a flow field affected by sidewall effects. The top view OF technique characterised the surface velocity field across the entire chute width, highlighting the occurrence of three-dimensional air-water surface patterns, although the data combined the surface flow motion across different free-surface elevations. One observed limitation of the OF was the requirement of a high frame rate (i.e. 10,000 fps or more) with some adequate high-quality light source. Despite these limitations, the combination of the three techniques provided a comprehensive understanding of the physical processes involved in self-aerated spillway flows, actively affecting energy dissipation and leading to a more efficient design of hydraulic structures. Further, the present study based upon a series of independent techniques demonstrated a successful complementary approach for sound air-water flow velocity measurements in high-velocity strongly-turbulent free-surface flows.

CRediT authorship contribution statement

Yvan Arosquipa Nina: Methodology, Software, Validation, Formal analysis, Investigation, Data curation, Writing – review & editing, Visualization. **Rui Shi:** Methodology, Software, Resources, Writing – review & editing, Supervision. **Davide Wüthrich:** Conceptualization, Methodology, Writing – review & editing, Supervision. **Hubert Chanson:** Conceptualization, Methodology, Validation, Resources, Writing – original draft, Writing – review & editing, Visualization, Supervision, Project administration, Funding acquisition.

Declaration of Competing Interest

The authors declare that they have no known competing financial interests or personal relationships that could have appeared to influence the work reported in this paper.

Digital Appendix I

Video movies of air-water flows on the stepped chute were recorded at real-time speed (Table A1). Movies M1, M2 and M3 show some skimming flows with different cavity shapes, i.e. ratio of cavity length to depth λ/k = 2.0, 2.5, 3.0 respectively. The Movie M4 presents a top view of the non-aerated flow and air-water flow region. Table S1 lists the details of the experimental flow conditions for each movie.

Table A1
Movies of skimming flows on air-water flows on stepped chute.

Movie	Filename	Camera	Movie details	Flow conditions	Description
M1	C0002.mp4	Sony RX100M5A	1920 × 1080 pixels (Movie mode 100 M/100p), 30 fps	Q = 0.163 m³/s, d_c/h = 1.4, Re = 6.5 × 10⁵, λ/k = 2.0	Air-water and cavity flow between step edges 8 and 10
M2	C0008.mp4	Sony RX100M5A	1920 × 1080 pixels (Movie mode 100 M/100p), 30 fps	Q = 0.098 m³/s, d_c/h = 1.0, Re = 3.9 × 10⁵, λ/k = 2.5	Air-water and cavity flow between step edges 7 and 9
M3	C0010.mp4	Sony RX100M5A	1920 × 1080 pixels (Movie mode 100 M/100p), 30 fps	Q = 0.130 m³/s, d_c/h = 1.2, Re = 5.2 × 10⁵, λ/k = 3.0	Air-water and cavity flow between step edges 8 and 10
M4	C0014.mp4	Sony RX100M5A	1920 × 1080 pixels (Movie mode 100 M/100p), 30 fps	Q = 0.130 m³/s, d_c/h = 1.2, Re = 5.2 × 10⁵, λ/k = 3.0	Top view of stepped chute overflow, incl. inception point and air-water flow

Digital Appendix II

Photographs of air-water flow features on the stepped chute were undertaken with a dSLR Pentax™ K-3, a digital camera Sony™ RX100M5A and a digital camera Casio™ EX-10 Exilim (Figs. A1 & A2). Figure A-1 shows photographs of the experimental facility, while Figure A-2 presents a number of high-speed photographs of air-water features.

Appendix A. Supplementary material

Supplementary data to this article can be found online at https://doi.org/10.1016/j.expthermflusci.2021.110545.

References

[1] E.H. Adelson, C.H. Anderson, J.R. Bergen, P.J. Burt, J.M. Ogden, Pyramid methods in image processing, RCA Eng. 29 (6) (1984) 33–41.

[2] Y. Arosquipa Nina, R. Shi, D. Wüthrich, H. Chanson, Intrusive and non-intrusive air-water measurements on stepped spillways with inclined steps: a physical study on air entrainment and energy dissipation, Hydraulic Model Report No. CH121/21, School of Civil Engineering, The University of Queensland, Brisbane, Australia, 2021, 258 pages & 8 video movies. https://doi.org/10.14264/e3f4d48. ISBN 978-1-74272-348-8.

[3] W.D. Bachalo, Experimental methods in multiphase flows, Int. J. Multiphase Flow 20 (Suppl.) (1994) 261–295.

[4] D.B. BUNG, Zur selbstbelüfteten Gerinnenströmung auf Kaskaden mit gemässigter Neigung, Self-aerated skimming flows on embankment stepped spillways. Ph.D. thesis, University of Wuppertal, LuFG Wasserwirtschaft und Wasserbau, Germany, 2009, pp.292 (in German).

[5] D.B. Bung, Non-intrusive measuring of air-water flow properties in self-aerated stepped spillway flow, in: Eric Valentine, Colin Apelt, James Ball, Hubert Chanson, Ron Cox, Rob Ettema, George Kuczera, Martin Lambert, Bruce Melville, Jane

Sargison (Eds.), Proc. 34th IAHR World Congress, Brisbane, Australia, 26 June-1 July, Engineers Australia Publication, 2011, pp. 2380–2387.

[6] Bung, D.B., Valero, D., 2015. Image processing for bubble image velocimetry in self-aerated flows. In: Proc. 36th IAHR World Congress, The Hague, The Netherlands, 27 June–3 July, 8 pages (CD ROM).

[7] D.B. Bung, D. Valero, Optical flow estimation in aerated flows, J. Hydraul. Res. 54 (2016) 575–580, https://doi.org/10.1080/00221686.2016.1173600.

[8] D.B. Bung, D. Valero, Image processing techniques for velocity estimation in highly aerated flows: bubble image velocimetry vs. optical flow, in: Proc. 4th IAHR European Congress, Liege, Belgium, 2016b, pp. 151–157.

[9] D.B. Bung, D. Valero, FLOWCV – An open-source toolbox for computer vision applications in turbulent flows, in: Editors Aminuddin Ab. Ghani, Ngai Weng Chan, Junaidah Ariffin, Ahmad Khairi Abd Wahab, Sobri Harun, Amir Hashim Mohamad Kassim, Othman Karim (Eds.), Proceedings of 37th IAHR World Congress, IAHR & USAINS Holding Sdn. Bhd. Publ., Kuala Lumpur, Malaysia, 13–18 August, 10 pages.

[10] P. Cain, I.R. Wood, Instrumentation for aerated flow on spillways, J. Hyd. Div. 107 (11) (1981) 1407–1424.

[11] P. Cain, I.R. Wood, Measurements of self-aerated flow on a spillway, J. Hyd. Div. 107 (11) (1981) 1425–1444.

[12] G. Carosi, H. Chanson, Turbulence characteristics in skimming flows on stepped spillways, Can. J. Civil Eng. 35 (9) (2008) 865–880, https://doi.org/10.1139/L08-030.

[13] A. Cartellier, J.L. Achard, Local phase detection probes in fluid/fluid two-phase flows, Rev. Sci. Instrum. 62 (2) (1991) 279–303.

[14] M.R. Chamani, Air inception in skimming flow regime over stepped spillways, in: H.E. Minor, W.H. Hager (Eds.), Intl Workshop on Hydraulics of Stepped Spillways, Zürich, Switzerland, Balkema Publ., 2000, pp. 61–67.

[15] M.R. Chamani, N. Rajaratnam, Characteristics of skimming flow over stepped spillways, J. Hydraulic Eng. 125 (4) (1999) 361–368. Discussion: Vol. 126, No. 11, pp. 860–872. Closure: Vol. 126, No. 11, pp. 872–873.

[16] H. Chanson, Air Bubble Entrainment in Free-Surface Turbulent Shear Flows, Academic Press, London, UK, 1997, 401 pages.

[17] H. Chanson, The Hydraulics of Stepped Chutes and Spillways, Balkema, Lisse, The Netherlands, 2001.

[18] H. Chanson, Air-water flow measurements with intrusive phase-detection probes. Can we improve their interpretation? J. Hydraulic Eng. 128 (3) (2002) 252–255, https://doi.org/10.1061/(ASCE)0733-9429(2002)128:3(252).

[19] H. Chanson, Hydraulics of aerated flows: Qui Pro Quo? J. Hydraulic Res. 51 (3) (2013) 223–243, https://doi.org/10.1080/00221686.2013.795917. IAHR, Invited Vision paper.

[20] H. Chanson, Interactions between a developing boundary layer and the free-surface on a stepped spillway: Hinze Dam spillway operation in January 2013, In: Proc. 8th International Conference on Multiphase Flow ICMF 2013, Jeju, Korea, 26–31 May, Gallery Session ICMF2013-005 (Video duration: 2:15), 2013.

[21] H. Chanson, Phase-detection measurements in free-surface turbulent shear flows, J. Geophys. Eng. 13 (2) (2016) S74–S87, https://doi.org/10.1088/1742-2132/13/2/S74.

[22] H. Chanson, On optical flow technique: experience and commentary, in: Shi, R., Wüthrich, D., Chanson, H., (Eds.), Air-water characteristics of a breaking bore roller Part II: Air-water flow properties, Hydraulic Model Report No. CH118/20, School of Civil Engineering, The University of Queensland, Brisbane, Australia, Appendix G, 2021, 6 pages. ISBN 978-1-74272-339-6.

[23] H. Chanson, L. Toombes, Air-water flows down stepped chutes: turbulence and flow structure observations, Int. J. Multiphase Flow 28 (11) (2002) 1737–1761, https://doi.org/10.1016/S0301-9322(02)00089-7.

[24] C. Crowe, M. Sommerfield, Y. Tsuji, Multiphase Flows with Droplets and Particles, CRC Press, Boca Raton, USA, 1998, p. 471.

[25] R. Ehrenberger, Wasserbewegung in steilen Rinnen (Susstennen) mit besonderer Berucksichtigung der Selbstbelüftung, ('Flow of Water in Steep Chutes with Special Reference to Self-aeration.') Zeitschrift des Österreichischer Ingenieur und Architektverein, No. 15/16 and 17/18 (in German) (translated by Wilsey, E.F., U.S. Bureau of Reclamation), 1926.

[26] H.T. Falvey, Air-water flow in hydraulic structures, USBR Engineering Monograph, No. 41, Denver, Colorado, USA, 1980.

[27] G. Farnebäck, Two-frame motion estimation based on polynomial expansion, in: Proc. Scandinavian Conference on Image Analysis SCIA 2003, Springer, Berlin, Heidelberg, 2003, pp. 363–370.

[28] S. Felder, Air-Water Flow Properties on Stepped Spillways for Embankment Dams: Aeration, Energy Dissipation and Turbulence on Uniform, Non-Uniform and Pooled Stepped Chutes, Ph.D. thesis, School of Civil Engineering, The University of Queensland, Brisbane, Australia, 2013.

[29] S. Felder, H. Chanson, Energy dissipation, flow resistance and gas-liquid interfacial area in skimming flows on moderate-slope stepped spillways, Environ. Fluid Mech. 9 (4) (2009) 427–441, https://doi.org/10.1007/s10652-009-9130-y.

[30] C.A. Gonzalez, An Experimental Study of Free-Surface Aeration on Embankment Stepped Chutes, Ph.D. thesis, Department of Civil Engineering, The University of Queensland, Brisbane, Australia, 2005.

[31] R.A. Herringe, M.R. Davis, Detection of instantaneous phase changes in gas-liquid mixtures, J. Phys. E: Sci. Instrum. 7 (10) (1974) 807–812.

[32] B.K.P. Horn, B.G. Schunck, Determining optical flow, Artif. Intell. 17 (1-3) (1981) 185–203.

[33] O.C. Jones, J.-M. Delhaye, Transient and statistical measurement techniques for two-phase flows: a critical review, Int. J. Multiph. Flow 3 (2) (1976) 89–116.

[34] M. Kramer, H. Chanson, Optical flow estimations in aerated spillway flows: filtering and discussion on sampling parameters, Exp. Therm Fluid Sci. 103 (2019) 318–328, https://doi.org/10.1016/j.expthermflusci.2018.12.002.

[35] J. Leandro, D. Bung, R. Carvalho, Measuring void fraction and velocity fields of a stepped spillway for skimming flow using non-intrusive methods, Exp. Fluids 55 (2014), https://doi.org/10.1007/s00348-014-1732-6. Paper 1732, 17 pages.

[36] E. McCurdy, The Notebooks of LEONARDO DA VINCI. Jonathan Cape, London, UK, 6th ed., 2 vols., 1956.

[37] J. Matos, Onset of skimming flow on stepped spillways. Discussion, J. Hydraulic Eng. 127 (6) (2001) 519–521.

[38] L.S. Neal, S.G. Bankoff, A high resolution resistivity probe for determination of local void properties in gas-liquid flows, Am. Inst. Chem. J. 9 (1963) 49–54.

[39] N.S.L. Rao, H.E. Kobus, Characteristics of self-aerated free-surface flows, in: Water and Waste Water/Current Research and Practice, vol. 10, Eric Schmidt Verlag, Berlin, Germany, 1974, 224 pages.

[40] Y. Ryu, K.A. Chang, H.J. Lim, Use of bubble imaging velocimetry for measurement of plunging wave impinging on structure and associated greenwater, Measur. Sci. Technol. 16 (10) (2005) 1945–1953.

[41] R. Shi, D. Wüthrich, H. Chanson, Applications of optical flow technique in air-water flows, in: H. Chanson, R. Brown (Eds.), Proceedings of 22nd Australasian Fluid Mechanics Conference AFMC2020, Brisbane, Australia, 7–10 December, Published by The University of Queensland, 2020, Paper 21, 4 pages. https://doi.org/10.14264/d44ca31.

[42] R. Shi, D. Wüthrich, H. Chanson, Air-water characteristics of a breaking bore roller Part II: Air-water flow properties, Hydraulic Model Report No. CH118/20, School of Civil Engineering, The University of Queensland, Brisbane, Australia, 2021, 160 pages. ISBN 978-1-74272-339-6.

[43] L.G. Straub, A.G. Anderson, Experiments on self-aerated flow in open channels, J. Hydraulic Divis. Proc. 84 (HY7) (1958) paper 1890, pp. 1890-1–1890-35.

[44] L. Toombes, H. Chanson, Interfacial aeration and bubble count rate distributions in a supercritical flow past a backward-facing step, Int. J. Multiphase Flow 34 (5) (2008) 427–436, https://doi.org/10.1016/j.ijmultiphaseflow.2008.01.005.

[45] I.R. Wood, Air entrainment in free-surface flows, IAHR Hydraulic Structures Design Manual No. 4, Hydraulic Design Considerations, Balkema Publ., Rotterdam, The Netherlands, 1991, 149 pages.

[46] D. Wüthrich, R. Shi, H. Wang, Chanson, Three-dimensional air-water flow properties of a hydraulic jump with low Froude numbers and relatively high Reynolds numbers, in: R. Janssen, H. Chanson (Eds.), Proceedings of the 8th IAHR International Symposium on Hydraulic Structures ISHS2020, 12–15 May 2020, Santiago, Chile, The University of Queensland, Brisbane, Australia, 2020, 10 pages. https://doi.org/10.14264/uql.2020.583.

[47] D. Wüthrich, R. Shi, H. Chanson, Strong free-surface turbulence in breaking bores: a physical study on the free-surface dynamics and air-water interfacial features, Paper A20, 37 pages, J. Fluid Mech. 924 (2021), https://doi.org/10.1017/jfm.2021.614.

[48] J. Yang, C. Lin, M.J. Kao, P.H. Teng, R.V. Raikar, Application of SIM, HSPIV and BIV techniques for evaluation of a two-phase air-water chute aerator flow, Water 10 (2018). Paper 1590.

[49] Y. Yasuda, H. Chanson, Micro- and macro-scopic study of two-phase flow on a stepped chute, in: J. Ganoulis, P. Prinos (Ed.), Proc. 30th IAHR Biennial Congress, Thessaloniki, Greece, Vol. D, 2003, pp. 695–702.

[50] G. Zhang, 2017. Free-Surface Aeration, Turbulence, and Energy Dissipation on Stepped Chutes with Triangular Steps, Chamfered Steps, and Partially Blocked Step Cavities, Ph.D. thesis, The University of Queensland, School of Civil Engineering, 361 pages. https://doi.org/10.14264/uql.2017.906.

[51] G. Zhang, H. Chanson, Application of local optical flow methods to high-velocity air-water flows: validation and application to skimming flows on stepped chutes, Hydraulic Model Report No. CH105/17, School of Civil Engineering, The University of Queensland, Brisbane, Australia, 2017, 59 pages.

[52] G. Zhang, H. Chanson, Self-aeration in the rapidly- and gradually-varying flow regions of steep smooth and stepped spillways, Environ. Fluid Mech. 17 (1) (2017) 27–46, https://doi.org/10.1007/s10652-015-9442-z.

[53] G. Zhang, H. Chanson, Application of local optical flow methods to high-velocity free-surface flows: validation and application to stepped chutes, Exp. Therm Fluid Sci. 90 (2018) 186–199, https://doi.org/10.1016/j.expthermflusci.2017.09.010.